Department of Physics and Astronomy

University of Heidelberg

Master thesis

in Physics

submitted by

Alexander Egl

born in Aschaffenburg

2016

Commissioning of the offline transfer beamline for the ALPHATRAP experiment

This Master thesis has been carried out by Alexander Egl

at the

Max-Planck-Institut für Kernphysik in Heidelberg

under the supervision of

Prof. Dr. Klaus Blaum

Dr. Sven Sturm

Commisioning of the offline transfer beamline for the ALPHATRAP experiment:

The novel cryogenic Penning-trap experiment ALPHATRAP is currently set up at the Max-Planck-Institut für Kernphysik in Heidelberg. ALPHATRAP is a follow-up experiment of the Mainz g-factor experiment, extending measurements of the bound electron g-factor to the high-Z regime. This allows, among others for a high-precision test of bound-state quantum electrodynamics in the extremely strong fields of highly charged ions. Ions up to hydrogen-like $^{208}Pb^{81+}$ are externally produced in the Heidelberg electron beam ion trap (EBIT) and will be transferred in a ultra-high vacuum beamline to the Penning trap-setup.
The commissioning and setup of this beamline is the subject of this thesis. A second compact non-cryogenic EBIT is used as an offline ion source for the test and commissioning of the beamline and Penning-trap system. It was shown that with this compact EBIT, bunches of argon ions up to $^{40}Ar^{15+}$ can be extracted. For these ion bunches, the transport through the offline beamline and deceleration, necessary for the ion injection into the Penning-trap system, were successfully demonstrated. Results for charge-state distributions from the EBIT and the time of flight of the ion transport are presented.
For sympathetic laser cooling of the trapped ions in the future, the production of $^{9}Be^{+}$ in an external laser ablation source was demonstrated, and an interim in-trap ion source for the production of $^{9}Be^{+}$ was constructed.

Kommissionierung der Ionentransportstrecke für das ALPHATRAP Experiment:

Das neue kryogene Penningfallen-Experiment ALPHATRAP befindet sich derzeit im Aufbau am Max-Planck-Institut für Kernphysik in Heidelberg. Es ist der Nachfolger des Mainzer g-Faktor-Experiments und wird die Bestimmung des g-Faktors von gebundenen Elektronen in den Bereich höherer Ladungszustände erweitern. Dies ermöglicht es u.a. die Quantenelektrodynamik in gebundenen Zuständen von hoch geladenen Ionen mit höchster Präzision zu testen. Die hochgeladenen Ionen bis zu wasserstoffähnlichem $^{208}Pb^{81+}$ müssen extern in der Heidelberger Elektronenstrahl-Ionenfalle (EBIT) erzeugt werden. Für den Transport von der Heidelberg-EBIT zu der Penningfalle wird daher eine Beamline benötigt.
Gegenstand dieser Arbeit ist die Kommissionierung und der Aufbau dieser Ionentransportstrecke. Zur Inbetriebnahme und Testzwecken der Strahlführungslinie und des Fallensystems steht eine weitere kompakte nicht kryogene EBIT zur Verfügung. Es konnte gezeigt werden, dass von dieser EBIT hochgeladene Ionen bis zu $^{40}Ar^{15+}$ extrahiert, durch die Strahlführungslinie transportiert und für den Einschuss in die Penningfallen abgebremst werden können. Es werden Ergebnisse zu den Ladungszustandsverteilungen aus der EBIT und Flugzeitmessungen des Ionentransports präsentiert.
Für eine geplante sympathetische Laserkühlung der gefangenen Ionen wurde die Produktion von $^{9}Be^{+}$ in einer externen Laserablationsquelle gezeigt und für eine zwischenzeitliche in-situ Produktion von $^{9}Be^{+}$ in der Falle eine Ionenquelle konstruiert.

Contents

1 Motivation **5**

2 Theory **7**
2.1 The electron *g*-factor 7
2.1.1 The *g*-factor of the free electron 7
2.1.2 The *g*-factor of the bound electron 9
2.2 ALPHATRAP 10
2.3 *g*-factor measurements with Penning traps 13
2.3.1 The ideal Penning trap 14
2.3.2 Measurement principle 17

3 Experimental setup **21**
3.1 Room-temperature beamline vacuum system 21
3.2 Electron beam ion traps 23
3.3 Wien filter 27
3.4 Microchannel plate detector 28
3.5 Pulsed drift tube 29
3.6 Cryostat and magnet 30
3.7 Double Penning-trap system 32
3.7.1 The double-trap setup 32
3.7.2 Measurement procedure in a double-trap system 32
3.8 In-trap ion source 33

4 Results **36**
4.1 tt-EBIT characterization 37
4.2 Demonstration of ion transport 48
4.3 Conclusions 51
4.4 Laser ablation source for beryllium ions 53

5 Outlook **57**

6 Bibliography **59**

1 Motivation

Often the excitement for an experimental research is to test explanations and predictions of existing theories and aims to derive a deeper understanding and sophisticated knowledge of physics and the laws of nature. One way to do this consists in improving the precision of experiments in order to reach a level which poses a challenge to current models or predictions, where less known or unexpected phenomena might emerge. One example is the measurement of the electron g-factor , both for the free electron [1, 2] and of an electron bound to a nucleus [3–5]. This dimensionless quantity is a directly accessible observable in experiments. Its value can be predicted with an extreme accuracy by quantum electrodynamics (QED) [6–8], one of the most important fundamental theories of the Standard Model in contemporary physics. High-precision Penning-trap experiments are widely used to test those predictions and are useful tools for these kind of investigations. Currently the high-precision Penning-trap experiment ALPHATRAP is set up at the Max-Planck-Institut für Kernphysik, Heidelberg.

Penning traps allow the storage and investigation of a *single* charged particle. Unlike other similar high-precision g-factor experiments, ALPHATRAP is going to test QED in the regime of extremely high electric fields of up to $10^{18}\,\mathrm{V/m}$. The highest electric and magnetic fields which can be accessed in laboratory experiments are the fields electrons experience when bound to a nucleus. Hence in the ALPHATRAP experiment highly charged ions serve as a test object. By extending previously done experiments at the g-factor apparatus in Mainz [9] to even heavier highly charged ions, QED can be tested under extreme conditions. Whereas an in-trap creation of the highly charged ions was feasible in the g-factor apparatus in Mainz, external ion sources have to be used in the ALPHATRAP experiment for even heavier highly charged ions. As a consequence, a beamline and an external transport and injection system for the ions are needed. In the end of 2015 and the beginning of 2016, the ALPHATRAP experiment proceeded to the next phase and final constructions and assemblies were conducted.

In the second chapter a brief introduction to the basic theory of the free and bound electron g-factor is given. The high-precision Penning-trap experiment ALPHATRAP is motivated and the principles of the measurement with (ideal) Penning traps are explained.

In the third chapter the experimental setup of the ALPHATRAP experiment is presented. For the external production of the highly charged ions, electron ion beam traps (EBIT) are used. The principle of this ion source and all necessary components for an ion transfer beamline are explained.

The main aim of this thesis was to setup and commission the beamline before and after moving it from an offline test stand to its final position. The characterization of an EBIT and the demonstration for ion transport in the beamline system is presented as the main result of this thesis in the fourth chapter.

2 Theory

QED is a relativistic quantum field theory of electrodynamics. QED describes the interaction of charged particles with each other and with electromagnetic fields at all energies and field strengths. This interaction is mediated by the photons. In 1965 the Nobel Prize in Physics was awarded jointly to Sin-Itiro Tomonaga, Julian Schwinger and Richard P. Feynman "for their fundamental work in quantum electrodynamics" [10]. By using QED they were able to explain (experimentally observed) deviations from Dirac's theory, such as the Lamb shift in hydrogen [11] and the electron's anomalous magnetic moment - a deviation of its g-factor from 2. There are many high-precision experiments exploiting different approaches to test QED [2, 5, 12, 13]. Down to the present day all the experimental results are in agreement with theory. This makes QED one of the most accurate and most precisely tested theories of physics. Due to this success and its ability to predict the values of physical observables, QED serves as a model for other subsequent quantum field theories.

2.1 The electron g-factor

In the Standard Model, the electron is considered an elementary particle belonging to the group of leptons and supposedly lacking any substructure [14]. It has an intrinsic charge equal to an elementary charge e and it carries a spin[1] $\mathbf{s}$ of $1/2\hbar$. The magnetic moment $\boldsymbol{\mu}$ is related to its spin $\mathbf{s}$ via the dimensionless electron g-factor g_e in units of the Bohr magneton μ_B given by

$$\boldsymbol{\mu} = -g_e \frac{e}{2m_\mathrm{e}}\mathbf{s} = -g_e \frac{\mu_\mathrm{B}}{\hbar}\mathbf{s}, \tag{2.1}$$

where m_e denotes the electron mass and $\hbar = h/2\pi$ the reduced Planck constant.

2.1.1 The g-factor of the free electron

The value of the free electron g-factor was first calculated by Dirac in 1928 [15]. In his relativistic quantum mechanical treatment of the wave function of a massive spin-$1/2$ particle, g_e equals 2, which is the same as the 0^{th} order of perturbation in QED [14]. Experiments by Kusch and Foley in 1947 [16] were the first to show a deviation from the expected value of 2. The excess is called the "anomalous magnetic moment" of the electron and described by the quantity $a_e = \frac{1}{2}(g_e - 2)$. This deviation

[1] Bold faced letters denote vectorial quantities

agreed with QED calculation performed by Schwinger [17]. In the Standard Model, there are contributions from three types of interactions, electromagnetic, hadronic and electroweak:

$$a_e = \Delta a_e\,(\text{QED}) + \Delta a_e\,(\text{hadronic}) + \Delta a_e\,(\text{electroweak})\,. \tag{2.2}$$

In the framework of the Standard Model, the dominant contribution comes from $\Delta a_e\,(\text{QED})$, whereas $\Delta a_e\,(\text{hadronic})$ and $\Delta a_e\,(\text{electroweak})$ provide only small corrections. The deviation due to QED effects arises from the interaction of the electron with real or virtual electromagnetic fields. For a free electron the dominant contribution is due to self-energy and vacuum polarization. They must be taken into account when comparing the theoretical value with measurements [18]. Since the strength of the electromagnetic interaction is characterized by the fine structure constant α ($\simeq {}^{1}/_{137}$), the QED contributions can be perturbatively expanded in a power series of α. The order of the expansion herein corresponds to the number of vertices in the corresponding Feynman graphs [18]:

$$\Delta g_e\,(\text{QED}) = \sum_{n=1}^{\infty} \left(\frac{\alpha}{\pi}\right)^n a_e^{2n}, \tag{2.3}$$

$$= a_e^2 \left(\frac{\alpha}{\pi}\right) + a_e^4 \left(\frac{\alpha}{\pi}\right)^2 + a_e^6 \left(\frac{\alpha}{\pi}\right)^3 + a_e^8 \left(\frac{\alpha}{\pi}\right)^4 + a_e^{10} \left(\frac{\alpha}{\pi}\right)^5 + \ldots \tag{2.4}$$

The coefficients a_e^{2n} are finite due to the renormalizability of QED and also dependent on the mass m_μ resp. m_τ of the other two leptons in the Standard Model, the muon and tauon, as

$$a_e^{2n} = A_1^{2n} + A_2^{2n}({}^{m_e}/_{m_\mu}) + A_2^{2n}({}^{m_e}/_{m_\tau}) + A_3^{2n}({}^{m_e}/_{m_\tau}, {}^{m_e}/_{m_\mu}). \tag{2.5}$$

The first three terms of A_1^2, A_1^4, A_1^6 are known analytically, whereas the others are calculated numerically by taking an increasing number of Feynman diagrams into account[2]. The comparison between theoretical and experimental values for the free electron g-factor shows a good agreement:

$$a_{\text{e,free}}^{\text{theo}} = 1.159\ 652\ 181\ 643\ (25)\ (23)\ (16)\ (763)\ 10^{-3}\ [0.03\ \text{ppb}], \tag{2.6}$$

$$a_{\text{e,free}}^{\text{exp}} = 1.159\ 652\ 180\ 73\ \ (28)\ 10^{-3}\ [0.24\ \text{ppb}]. \tag{2.7}$$

To date the most precise[3] theoretical value (2.6) for the free electron g-factor was calculated by Aoyama et al. [18], where the first three uncertainties are from higher order QED, hadronic and electroweak contributions. The last and largest uncertainty is due to the uncertainty in the value of the fine structure constant[4] α. The most precise experimental value for the free electron g-factor (2.7) was measured in the Harvard g-2 experiment by Gabrielse et al. [2].

[2] e.g. 891 resp. 12672 Feynman diagrams contribute to the value of A_1^8 resp. A_1^{10} [18]

[3] Here [0.03 ppb] $\equiv$ 0.03 parts per billion $\equiv 0.03 \times 10^{-9}$ refers to the instrinsic theoretical relative uncertainty and does not take the uncertainty in α into account

[4] For consistency the best known value for α not determined by g-2 measurements must be used [13] (see also section 2.2).

2.1.2 The *g*-factor of the bound electron

For the description of the electron bound in the nuclear coulomb field of highly charged ions (HCI), additional effects contributing to the *g*-factor should be considered. These are summarized under the name of bound-state QED (BS-QED). The main contribution arises from relativistic corrections that can be solved analytically being a direct solution of the Dirac equation, describing an electron bound in the potential of a point charge with infinite mass. This was done by Breit in 1928 [19] and it is known as "Breit term". It reads for an electron in the 1s ground state of a hydrogen-like ion:

$$g_{\text{Breit}} = \frac{2}{3}\left(1 + 2\sqrt{1-(Z\alpha)^2}\right). \tag{2.8}$$

Being a rather small effect of a few ppm in a hydrogen atom, it reaches up to $\approx 13\%$ in hydrogen-like lead (Fig. 2.1). As in the case of the free electron *g*-factor, the QED

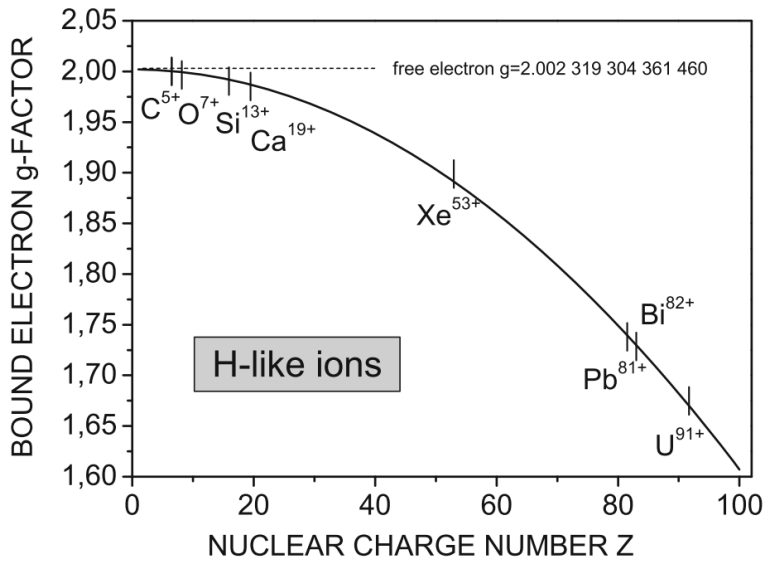

Figure 2.1: Breit term for to the bound electron *g*-factor for hydrogen-like ions with nuclear charge $Z = 1 - 92$ [14].

corrections for the bound electron *g*-factor are calculated as a series expansion in α. In addition the coupling to the *strong* electric field of the nucleus with nuclear charge Z has also to be taken into account. *Strong* herein refers to fields which cannot be considered as a small perturbation anymore. In contrast to the free electron, coupling to the field of the nucleus reads $Z\alpha$ instead of α. As an example, for hydrogen-like lead $^{208}Pb^{81+}$, $Z\alpha \simeq 0.60$ (instead of $\alpha \simeq 1/137 \simeq 0.007$). Therefore, the field has to be considered non-perturbatively in all orders and the corrections can be calculated numerically.

Even though the deviation from 2 for the bound electron g-factor is dominated by binding as well as nuclear and relativistic effects, the QED effects are not negligible in high Z systems. Testing these predictions is a strong motivation for precision g-factor measurements on HCI. So far only the one-loop QED contributions are calculated in all orders of $(Z\alpha)$. Whereas BS-QED calculations are most accurate for small Z, the dominant theoretical uncertainty arises from uncalculated two-loop diagrams of order $(Z\alpha)^5$ or higher (Fig. 2.2) [20]. As shown in Fig. 2.2, in low Z systems untested BS-QED contributions are on the level of 10^{-10} to 10^{-9}, whereas in the high Z regime untested effects occur already on the level of 10^{-6}. For higher values of Z, nuclear effects, for instance contributions due to the nuclear recoil and finite nuclear volume, become more significant. So far, the motion of the electron was assumed as to be in the constant central potential created by the nucleus being at rest. However, by improving the experimental resolution and sensitivity, this assumption is not longer justified. The nuclear recoil contribution is the leading mass-dependent term and the experimentally achieved accuracy in the ppb range for g-factor measurements would be sensitive enough for this effect [21], as in the case of isotopic dependencies [22]. Also, nuclear size and volume effects beyond a simple spherical model play a role. However they influence the g-factor value already in medium Z systems at the current level of experimental resolution [23]. All these contributions and their dependences on the nuclear charge Z are summarized in Fig. 2.2.

2.2 ALPHATRAP

One experimental method to measure the g-factor is the use of Penning traps such as ALPHATRAP. In the following, both a motivation for the ALPHATRAP experiment and an introduction to the principle of Penning traps shall be given. Hitherto, bound electron g-factor measurements were done for low Z systems such as $^{12}C^{5+}$ [3], $^{16}O^{7+}$ [4], $^{28}Si^{11+}$ [25], $^{28}Si^{13+}$ [5] and $^{40}Ca^{17+}$-$^{48}Ca^{17+}$ [22] at the University of Mainz. Up to date, the latter is the most stringent test of BS-QED at a level of 5×10^{-10} [5].

Today the current knowledge of the perturbative regime of QED is quite advanced and tested with extraordinary precision. However, less is known about the nonperturbative regime of QED when considering QED in very strong fields [26]. As for any perturbative theory, it is expected that QED might fail under extreme conditions. In fact, QED might be an effective theory that follows from the low-field limit of a more general theory. Therefore, pushing tests of QED to the extreme is of great interest. Nonlinear behavior for the electromagnetic field is supposed to occur[5] above a critical threshold for the electrical field strength (see E_{crit} in Fig. 2.3) [27, 28]. HCI are predestined objects, given that a *single* electron bound to the nucleus (*hydrogen-like* electron

[5]Note that these predictions were made under the assumption of a homogeneous electric field, whereas the Coulomb field of the nucleus has a spatial dependence.

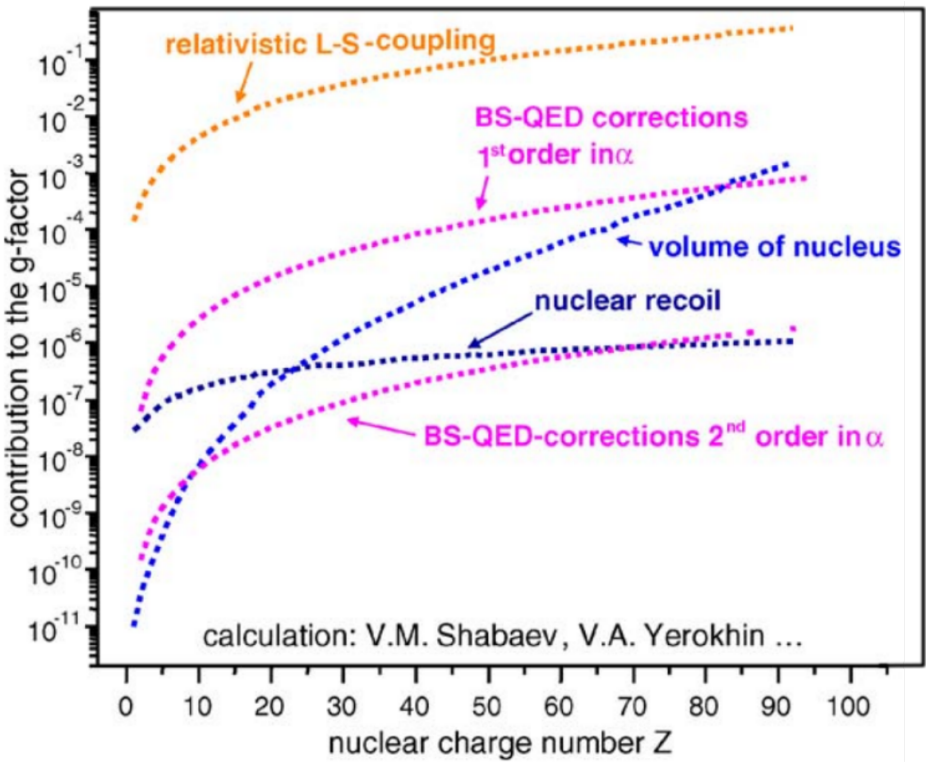

Figure 2.2: Contribution to the g-factor in hydrogen-like HCI with nuclear charge $Z = 1 - 90$ [24].

configuration, $1s^1$) experiences very strong electrical field strengths, which are not accessible otherwise experimentally. For instance in case of hydrogen-like $^{208}Pb^{81+}$, the expectation value of the electric field strength in the 1s state reaches 10^{16} V/cm (Fig. 2.3) [29]. ALPHATRAP aims to extend present measurements to the heavier ions. Considering high-Z systems and reaching higher accuracy, corrections due to the nuclear recoil and finite nuclear size or charge radius are also increasing. As the expectation value $\langle r \rangle$ of the nucleus-electron distance is approximately $\propto 1/z$ and the probability $|\psi(r = 0)|^2$ to find the electron at the center of the nucleus is $\propto Z^3$ [14], the nuclear properties are probed by the electron experiencing extreme electric and magnetic field strengths, which allows to draw conclusions about respective nuclear properties [22]. As laboratory system, electrons in the electric field of HCI up to hydrogen-like $^{208}Pb^{81+}$ will be used. Whereas in the aforementioned experiments with the Mainz setup, it was possible to use an in-trap ion source[6] with an electron beam energy of 4 keV to create hydrogen-like Si-ions, the very high ionization energies up to 100 keV [30] for hydrogen-like lead require an external production of the HCIs. Thus, one of the special features in the ALPHATRAP experiment is the possibility of

[6] See also section 3.8.

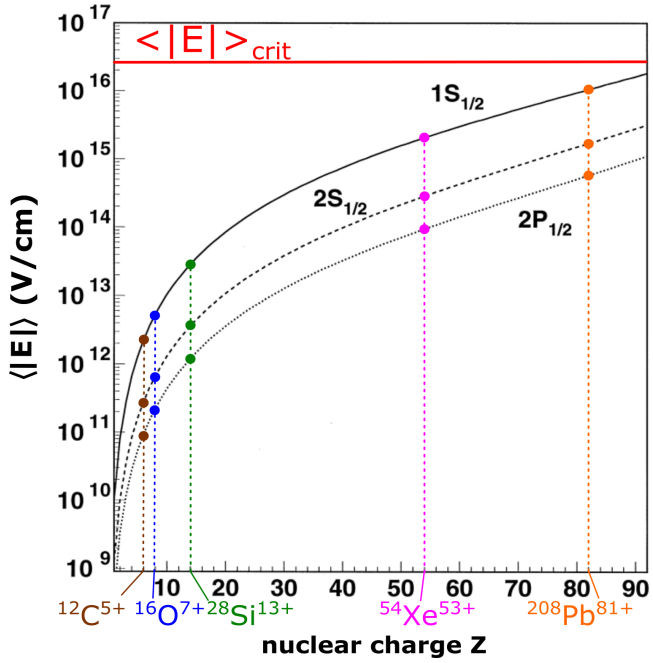

Figure 2.3: Expectation value of the electrical field strength for the lowest-lying states of a hydrogen-like ion in the range $Z = 1 - 92$ [29]. The red line denotes the critical field strength, where nonlinear behavior of the electromagnetic field is predicted. The first three ion species were measured in the Mainz g-factor experiments, where the other ones are candidates to be measured in the ALPHATRAP experiment.

external ion injection into the trap and a beamline for the transportation of the HCIs. Therefore, an ultra high to extremely high vacuum (UHV-XHV) room temperature transfer beamline is used to guide highly charged ions to a custom-made cryostat and a superconducting magnet containing the Penning-trap setup. HCIs can be provided by the Heidelberg Electron Beam Ion Trap (Heidelberg EBIT) of the group of José Crespo [31] located next to the ALPHATRAP setup and by a small non-cryogenic EBIT (section 3.2) [32].

In addition, the measurements of the g-factor on HCI would provide access to fundamental physical quantities such as the electron mass [33] and the fine structure constant α. The value of α can not be predicted by theory, but its precise determination is essential for the comparison of theoretical models with experimental observations. The dimensionless fine structure constant sets the scale of electromagnetic interaction and is of fundamental importance in physics, since it is also related

to other fundamental constants. The current 2014 CODATA[7] value is given as

$$\alpha^{-1}_{\text{CODATA14}} = 137.035\ \ 999\ \ 139\ \ (31)\ \ [0.23\ \text{ppb}]\ \ [34]. \tag{2.9}$$

In the theoretical value of the anomalous magnetic moment of the free electron (2.6), the intrinsic theoretical uncertainty of $\approx 38 \times 10^{-15}$ is $1/20$ of the uncertainty due to the fine structure constant α [18]. So by assuming the theoretical QED calculations and the Standard Model are correct, it is possible to deduce a value for α. By taking the best known values for the theoretical (2.6) and experimental values (2.7), the following value is obtained:

$$\alpha^{-1}_{\text{Harvard08}} = 137.035\ \ 999\ \ 084\ \ (51)\ \ [0.37\ \text{ppb}]\ \ [2]. \tag{2.10}$$

The best available value for the fine structure constant α determination with an independent method is obtained by the measurement of the recoil velocity of a Rb atom in an optical lattice upon absorption of a photon [13]. This is in agreement with the value in (2.10):

$$\alpha^{-1}_{\hbar/m(\text{Rb})} = 137.035\ \ 999\ \ 037\ \ (91)\ \ [0.66\ \text{ppb}]\ \ [13]. \tag{2.11}$$

g-factor measurements in HCI can provide an additional access to the fine structure constant, yielding an improved value for it. By comparing experimental and theoretical values for the bound electron g-factor in hydrogen-like ions, a value for α can be derived and its relative uncertainty can be approximated by [35]

$$\frac{\delta\alpha}{\alpha} \approx \frac{1}{(Z\alpha)^2}\sqrt{(\delta g_{\text{exp}})^2 + (\delta g_{\text{theo}})^2}. \tag{2.12}$$

Thus, for a given experimental uncertainty δg_{exp}, HCI with higher Z are favored. Nevertheless, for these high Z systems, the theoretical uncertainty δg_{theo} also increases significantly with Z, due to contributions from uncalculated higher order QED corrections and nuclear effects. Since the ultimate limit for the calculation of the bound electron g-factor is set by nuclear effects, Shabaev et al. proposed a method to reduce the achievable uncertainty for α significantly. This is based on the combination of g-factor measurement for boron[8]- and hydrogen-like ions of the same spinless high Z isotope [35]. The idea is based on the cancellation of contributions so that the uncertainty due to nuclear effects decreases, whereas the main α-dependent terms do not cancel (for a detailed description see [35]).

2.3 g-factor measurements with Penning traps

One way to test QED are high-precision experiments in Penning traps. The Penning trap allows to spatially confine charged particles and enables investigations by means

[7] Committee on Data for Science and Technology
[8] electron configuration $1s^2 2s^2 2p^1$

of radio frequency spectroscopy techniques. Therefore, this kind of trap is particularly well suited to high-precision experiments. Experiments were pioneered by Van Dyck, Schwinberg and Dehmelt at the University of Washington by the measurement of the free electron g-factor to a precision of 4×10^{-12} in 1987 [1], which was refined to a precision of 0.76×10^{-12} in 2008 by the group of Gabrielse at Harvard [2]. The Nobel Prize in Physics 1989 was awarded jointly to Hans G. Dehmelt and Wolfgang Paul "for the development of the ion trap technique" [36].

2.3.1 The ideal Penning trap

A Penning trap can be used to spatially confine charged particles by the superposition of static magnetic and electric fields. Being able to confine a particle in all three dimensions solely by means of an electrostatic field, it must be constructed in a way that, a potential energy minimum is established in space and therefore the corresponding force is pointing onto this point in all three directions. Earnshaw's Theorem states that such an electrostatic field does not exist [37]. A superposition of an electrostatic and a static magnetic field offer a way out of this problem. For the easiest analytical treatment this force $\boldsymbol{F}$ is harmonic and can then be written as the gradient of the potential energy U.

$$\boldsymbol{F} = -\nabla U(x, y, z). \tag{2.13}$$

Therefore, the potential energy has a quadratic dependency in the x, y, z coordinates.

$$U(x, y, z) = Ax^2 + By^2 + Cz^2, \tag{2.14}$$

where A, B, C are constants. For trapping a particle with charge q by an electrostatic field, U can be rewritten as $U = q\Phi$,

$$\Phi(x, y, z) = \frac{\Phi_0}{2d^2}\left(Ax^2 + By^2 + Cz^2\right), \tag{2.15}$$

Φ being the scalar electric potential and the characteristic trap parameter

$$d^2 = \frac{1}{2}\left(z_0^2 + \frac{\rho_0^2}{2}\right), \tag{2.16}$$

with the parameters z_0 and ρ_0 depending on the trap geometry.
The potential Φ (2.15) also has to satisfy the Laplace equation

$$\Delta U(x, y, z) = 0, \tag{2.17}$$

which is fulfilled when $A + B + C = 0$. The interesting case of rotational symmetry around the z-axis implies $A = B$ and $C = -(A + B)$ which leads to an electric quadrupole potential, for $A = -1/2$:

$$\Phi(x, y, z) = \frac{\Phi_0}{2d^2}\left(z^2 - \frac{(x^2 + y^2)}{2}\right) = \frac{\Phi_0}{2d^2}\left(z^2 - \frac{\rho^2}{2}\right), \tag{2.18}$$

where $\rho = \sqrt{x^2 + y^2}$ is the radius in cylindrical coordinates. The difference in signs of the radial and axial terms implies the potential has a saddle point and therefore confining along the axial coordinate while repulsive along the radial direction. To ensure confinement in the other coordinate, it is possible to use a static magnetic field (e.g. in the z-direction along the axis of rotational symmetry), leading to an (ideal) Penning trap [38].

The best approximation[9] of this field in a Penning trap configuration can be achieved by using a ring electrode and two endcap electrodes with a hyperbolic shape resembling the equipotential surfaces of the potential (Fig. 2.4 (a)). The first Penning traps were built in this geometry by Dehmelt in 1959, inspired by the experimental work of Penning in the 1930s [39]. Another geometrical realization can be achieved by using cylindrical annular electrodes, which are easier to machine and allow better access to the center of the trap (Fig. 2.4 (b)). Additional correction electrodes are used to remove and tune electrical field anharmonicities as proposed by Gabrielse [40].

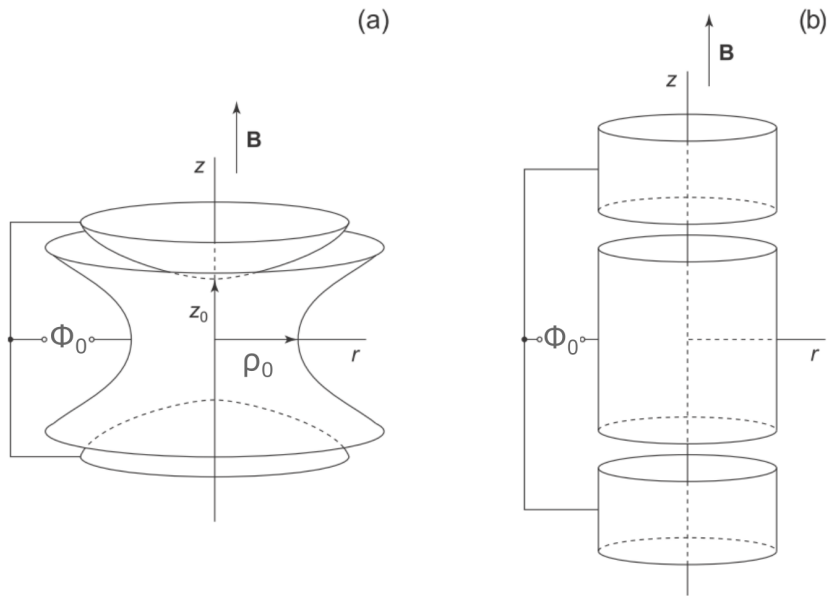

Figure 2.4: Schematics of Penning traps in (a) hyperbolic and (b) cylindrical electrodes geometry. The homogeneous magnetic field is aligned in z-direction [41].

To solve the equation of motion [38, 42] of a charged particle with mass m and charge q confined in an (ideal) Penning trap, it is instructive to separate the motion into independent axial and radial components. The equation of motion for the axial

[9] Apart from machining imperfections and finite size of the trap

and radial coordinates reads

$$m\ddot{z} = qE_z \tag{2.19}$$

$$m\ddot{\boldsymbol{\rho}} = q\left(\boldsymbol{E}_\rho + \dot{\boldsymbol{\rho}} \times \boldsymbol{B}\right). \tag{2.20}$$

E_z and $\boldsymbol{E}_\rho$ denote the components of the electric field in z and radial directions and the magnetic field is given by $\mathbf{B}$. Since the axial confinement in the z-direction is solely done by the electrostatic potential (2.18) and decoupled from the magnetic field pointing in the z-direction, a simple harmonic oscillation due to purely electrostatic forces along this z-direction is obtained,

$$\ddot{z} + \omega_z^2 z = 0 \tag{2.21}$$

with the axial angular frequency[10]

$$\omega_z = \sqrt{\frac{q\Phi_0}{md^2}}. \tag{2.22}$$

In the radial x-y-plane the restoring force results from the Lorentz force due to the magnetic and electrostatic fields (2.20). Thus, the result for the radial motion is a superposition of two harmonic oscillations with the magnetron frequency ω_- and the modified cyclotron motion with frequency ω_+:

$$\omega_\pm = \frac{\omega_c}{2} \pm \sqrt{\frac{\omega_c^2}{4} - \frac{\omega_z^2}{2}}, \tag{2.23}$$

where

$$\omega_c = \frac{q}{m}B \tag{2.24}$$

is the free cyclotron frequency. B denotes the constant homogeneous component of the magnetic field along the z-axis equal to the symmetry axis for the (ideal) Penning trap. Since the electrostatic potential is confining in the z-direction, the saddle-point shape in the radial x-y-plane causes a repulsion in radial direction. Therefore the (free) cyclotron frequency ω_c is reduced to the modified cyclotron frequency ω_+ because this repulsion reduces the centrifugal force. Some useful relations between these frequencies are:

$$\omega_+ + \omega_- = \omega_c, \tag{2.25}$$

$$2\omega_+\omega_- = \omega_z^2, \tag{2.26}$$

$$\omega_c > \omega_+ \gg \omega_z \gg \omega_-, \quad \text{(typically)} \tag{2.27}$$

$$\omega_+^2 + \omega_-^2 + \omega_z^2 = \omega_c^2. \tag{2.28}$$

[10] In the following ω denotes angular frequencies. They are related to the measured frequencies ν as: $\omega = 2\pi\nu$.

The latter is the so-called Brown-Gabrielse invariance theorem [42] which even holds in first order for a real Penning trap suffering from certain unavoidable imperfections[11]. Fig. 2.5 shows both the single trajectories of these eigenmotions as well as the resulting trajectory as the superposition of these three motions.

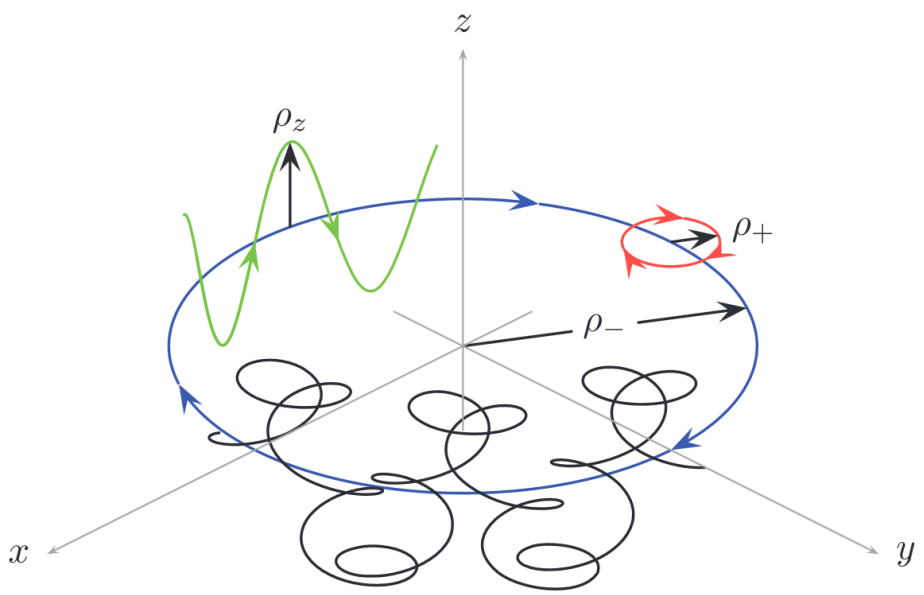

Figure 2.5: Exemplary motion of a charged particle in a Penning trap. ρ_+, ρ_- and ρ_z are the radii of the corresponding modified cyclotron (red), magnetron (blue) and axial (green) motion. The black line shows the resulting trajectory being a superposition of all three eigenmotions. The frequencies and amplitudes are not to scale [43].

2.3.2 Measurement principle

The measurement of the g-factor requires to measure different quantities to a high-precision themselves. The basic principle of a g-factor determination reads as follows:

As seen in the previous section, an ion in the Penning trap can be associated with a free cyclotron frequency ω_c (equation (2.24) which depends on the strength of the magnetic field B. This frequency ω_c can be determined measuring the frequencies ω_-, ω_+ and ω_z of the three eigenmotions and applying the invariance theorem (2.28). These frequencies of the ion motion can be measured non-destructively via an image-current detection and coupling different modes by radio frequency excitations. By the

[11] Equation (2.28) is exact even when the magnetic field and trap axis are misaligned provided the magnetic field is homogeneous and the electric potential purely quadrupolar.

ion motion in the trap, the oscillating charge induces currents in the trap electrodes. These currents in the fA-range can be measured via cryogenic amplifiers and resonant circuits developed in the group (see [44, 45] and references therein). At the same time, the unknown magnetic field strength is probed by measuring the Larmor frequency of the electron. During the measurement of the motional frequencies, spin flips are induced via microwave irradiation. The spin state can be analyzed through a non destructive spin state detection using the continuous Stern-Gerlach effect in the Analysis Trap (AT) of the Penning-trap system (see section 3.7) [14]. This was proposed by Dehmelt in 1973 [46] and successfully applied to electrons in a Penning trap three years later [47].

Continuous Stern-Gerlach effect

For an ion in a magnetic field the spin state degeneracy for the energy eigenstates is lifted. Since an electron in a magnetic field can have two spin eigenstates which differ in their energy by a value of ΔE, a total energy of $E_\pm = E_0 \pm \frac{1}{2}\Delta E$ can be assigned to the ion. E_0 denotes the energy due to the oscillatory motions and can be written as the sum of three independet quantum mechanical oscillators[12]:

$$E_0 = (n_+ + \frac{1}{2})\hbar\omega_+ - (n_- + \frac{1}{2})\hbar\omega_- + (n_z + \frac{1}{2})\hbar\omega_z. \tag{2.29}$$

n_i denotes the quantum number for one of the tree eigenmotions (+ = modified cyclotron, - = magnetron, z = axial) at their respective frequencies ω_i. ΔE is the Zeeman splitting for the energy eigenstates of the electron and proportional to the Larmor frequency ω_L

$$\Delta E = \hbar\omega_\mathrm{L} = \hbar\frac{g}{2}\frac{e}{m_\mathrm{e}}B, \tag{2.30}$$

which equals the precession frequency of the angular momentum of the electron with a magnetic dipole moment in the magnetic field.
The general shape of the magnetic field can be written as

$$B(z,\rho) = B_0 - 2B_1 z + B_2\left(z^2 - \frac{1}{2}\rho^2\right) + \ldots, \tag{2.31}$$

where B_0 is the homogeneous field, $B_1(z)$ a linear gradient along the z-direction and $B_2(z,\rho)$ a curvature describing the "magnetic bottle" (see Fig. 2.6 (a) and section 3.7). If $B_2 \neq 0$ the motional eigenfrequencies are shifted depending on their energies and the spin state of the electron [14]. For the axial motion, this can be seen in the following.

The potential energy Φ_mag of a magnetic moment $\boldsymbol{\mu}$ in a magnetic field $\boldsymbol{B}$ is given by

$$\Phi_\mathrm{mag} = -\boldsymbol{\mu}\boldsymbol{B}. \tag{2.32}$$

[12] Note the minus sign for the energy of the magnetron mode. This implies a reduction of this energy leads to an increase in the amplitude and results in a possible lose of the ion.

Neglecting the linear gradient in (2.31) and using (2.32), Φ_{mag} becomes spin state dependent, since there exist two eigenstates for the electron in a magnetic field:

$$\Phi_{\text{mag}} = -\mu_z^{\pm}\left(B_0 + B_2\left(z^2 - \frac{1}{2}\rho^2\right)\right), \tag{2.33}$$

where $\mu_z^{\pm}$ is the expectation value of the projection of the magnetic moment onto the z-axis. Thus in the z-direction the magnetic bottle contributes in addition to the present quadratic electrostatic potential Φ_{el}^z (2.18) a spin dependent quadratic potential Φ_{mag}^z, resulting in the effective axial potential Φ_{eff}^z (Fig. 2.6 (b)).

$$\Phi_{\text{eff}}^z = \Phi_{\text{el}}^z + \Phi_{\text{mag}}^z = \left(\frac{\Phi_0}{2d^2} \pm \mu_z B_2\right) z^2. \tag{2.34}$$

Therefore ω_z, determined by the total axial potential depends on the spin state of the electron. A spin flip results in a tiny shift $\Delta\omega_z$ which can be measured for the determination of the spin state,

$$|\Delta\omega_z| \approx \frac{B_2 g_e \mu_B}{m_{\text{ion}}\omega_z}. \tag{2.35}$$

The largest frequency differences are obtained with light hydrogen-like ions in a shallow trap and a strong magnetic bottle. The unambiguous detection of the spin flips is experimentally challenging since they cause relative frequency shifts $\Delta\omega_z/\omega_z$ in the order of 10^{-7}, e.g. for [5]. Technically limited drifts in the stability or noise of the trapping voltages cause already axial frequency shifts (2.35) in the same order of magnitude, making it more complicated to distinguish these from frequency shifts induced by spin flips. These are hurdles to overcome for measurements with heavier ions, since from (2.35) follows $\Delta\omega_z \propto \sqrt{\frac{1}{m_{\text{ion}}}}$.

Using the continuous Stern-Gerlach effect allows a non-destructive detection of the spin state. The maximum spin flip probability appears at a frequency equal to ω_{L} in the ideal case [44]. The Larmor frequency can be determined from the statistics of the spin flip probability by repeating this cycle many times at different micro wave excitation frequencies around ω_{L}.

By combining (2.30) and (2.24) one can determine the bound electron g-factor as:

$$g = 2\frac{\omega_{\text{L}}}{\omega_{\text{c}}}\frac{q_{\text{ion}}}{e}\frac{m_{\text{e}}}{m_{\text{ion}}} = 2\Gamma_0\frac{q_{\text{ion}}}{e}\frac{m_{\text{e}}}{m_{\text{ion}}}, \tag{2.36}$$

where $\Gamma_0 = \frac{\omega_{\text{L}}}{\omega_{\text{c}}}$. For the calculation of the g-factor the masses of the electron m_{e} and the ion m_{ion} are used as input parameters. Their uncertainties then contribute to the overall uncertainty of g and can also limit the achievable precision. A detailed scheme of the measurement procedure can be found in [44, 48].

Assuming the QED calculations are correct on their level of precision, one can rearrange equation (2.36) and use it to calculate the electron mass, being a fundamental constant in the Standard Model,

$$m_{\text{e}} = \frac{g}{2\Gamma_0}\frac{e}{q_{\text{ion}}}m_{\text{ion}}. \tag{2.37}$$

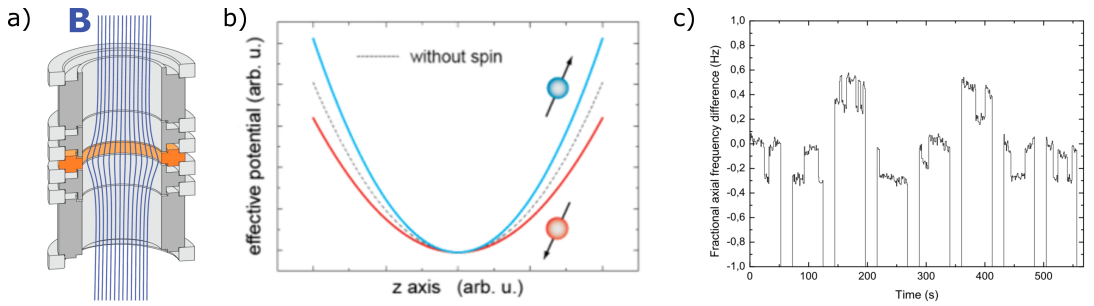

Figure 2.6: (a) Magnetic bottle due to the field distortions created by a ferromagnetic ring electrode (orange) (b) Dependence of the effective axial potential Φ^z_{eff} due to the interaction of the spin of the electron in hydrogen-like ions with a field inhomogeneity B_2 created by the magnetic bottle (c) Spin state detection in the AT with intermittent transport to the PT, where the spin transition is probed. Spinflips can be detected by observing the spin state before and after each stay in the PT. The changes in the absolute frequency are caused by changes of the cyclotron energy in the PT. The data is taken from [44] and similar observations are anticipated to be observed in the ALPHATRAP experiment.

This was done by Sturm et al. [33, 49, 50] by measuring the g-factor in hydrogen-like $^{12}C^{5+}$ surpassing the CODATA literature value [34] by a factor of 13 and it is used for the adjustments of the value for the electron mass m_e.

3 Experimental setup

This chapter will provide an overview of the ALPHATRAP setup with a particular focus on experimental tools that have been used in the course of this thesis. The ALPHATRAP experiment pushes *g*-factor measurements towards heavier systems. The ionization energies of the HCIs require an ex-situ production, feasible in electron beam ion traps (EBIT). The EBIT used for the ALPHATRAP experiment is the Heidelberg EBIT (HD-EBIT) [51, 52] at the Max-Planck-Institut für Kernphysik. The HD-EBIT will be able to produce HCI up to hydrogen-like lead $^{208}Pb^{81+}$. The cryogenic Penning-trap system of ALPHATRAP will be connected to the HD-EBIT via an ultra-high vacuum beamline. In the following sections, the operation principle of an EBIT, ion-optical elements employed in the beamline, the cryostat, the magnet and the Penning-trap system will be presented.

3.1 Room-temperature beamline vacuum system

A high-precision *g*-factor measurement in the Penning traps requires the ions to be stored for time in the order of weeks to months. To avoid collisions with ambient rest gas atoms causing charge exchange processes with the consequent change in the charge state of the trapped HCI, it is crucial to provide a sufficiently low pressure. Thus a pressure $\leq 10^{-16}$ mbar is mandatory [21]. This is achieved by using the cryopump and cryotrapping effect. The trap itself is cooled down to liquid helium temperatures of about 4.2 K. Since the Penning trap region is not an enclosed volume and is connected to the room temperature beamline via a CF16[1] tube, it is favorable to avoid heat radiation and influx of gas molecules from this section into the trap region. Therefore, on the one hand, a cryogenic valve was developed [54], which allows to separate the trap region from the remaining beamline and is fully operational at a temperature of 4.2 K and at high magnetic field strength. On the other hand, it is desirable to achieve pressures as low as possible already in the room temperature section of the beamline. The main section of the room temperature beamline is made CF160 components and it is equipped with different sort of vacuum pumps providing the required pumping power (Tab. 3.1).

[1] CF flanges use copper gasket and knife-edge flange for sealing. ConFlat™ by Varian [53].

Table 3.1: Overview of the used vacuum pumps for the ultra-high vacuum section of the beamline. TP= turbomolecular pump, NEG=Non-Evaporable Getter pump, IGP= ion getter pump.

Label (Fig. 3.1)	Type	Manufacturer	Model	Maximum Pumping Speed (l/s)
Wien filter	TP	Edwards [55]	nEXT300D	350 (N_2)
DD	TP	Edwards	STP-603	650 (N_2)
Bender	TP	Edwards	STP-603	650 (N_2)
IO1a	TP	Edwards	STP-603	650 (N_2)
IO1b	TP	Edwards	STP-603	650 (N_2)
NEG1	NEG	SAES [56]	CapaciTorr C2000	2000 (H_2)
IGP	IGP	Agilent [57]	VacIon Plus 500	410 (N_2)
NEG2	NEG+ IGP	SAES	NEXTorr D2000-10	2000 (H_2)

The schematics for the ultra-high vacuum section of the beamline is shown in Fig. 3.1. Additionally, all stainless steel (316LN) components of the beamline are vacuum fired to reduce H_2 outgassing [58] and later on the beamline will be in-situ baked to 300 °C.

In addition to the HD-EBIT and for commissioning purposes, a smaller table top EBIT (tt-EBIT) developed in the group of José Crespo [32], is available. The tt-EBIT allows a flexible creation of highly charged ions of moderately heavy elements from injected gas (e.g. $^{40}Ar^{15+}$ or $^{129}Xe^{25+}$).

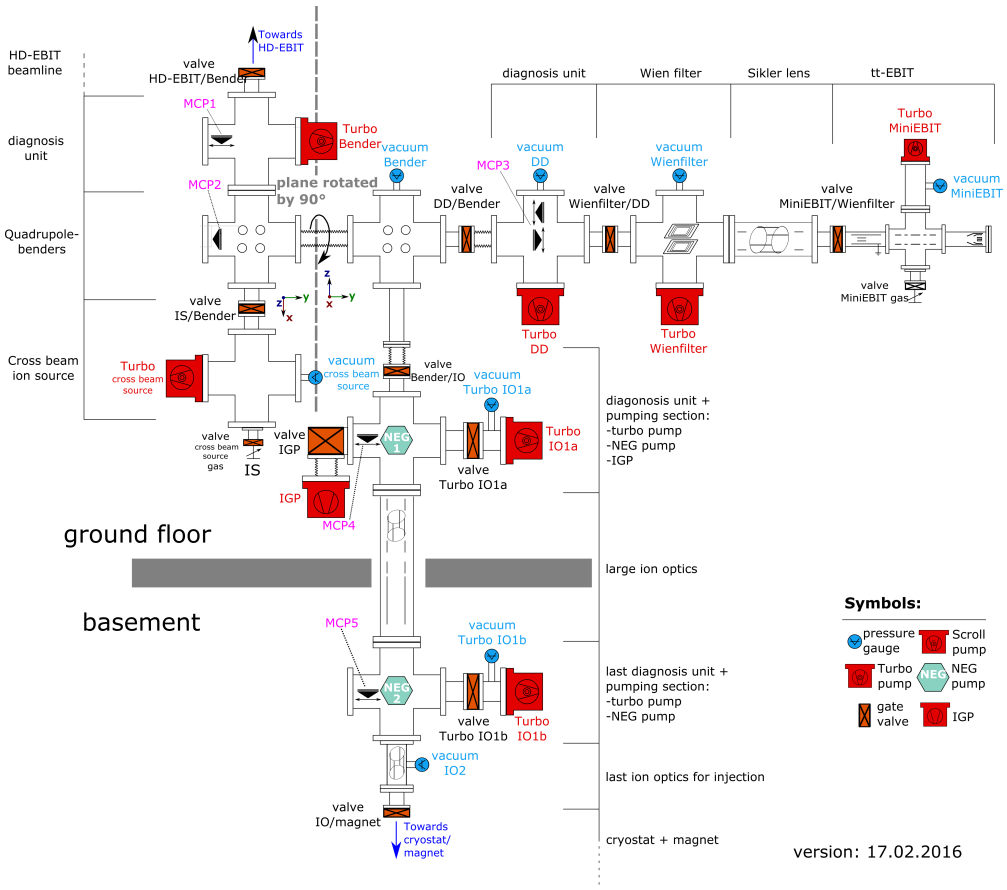

Figure 3.1: Schematic overview of the UHV beamline of the ALPHATRAP setup as build up in the context of this thesis. IO=ion optics, IS=cross beam ion source.

3.2 Electron beam ion traps

EBITs produce HCI through electron impact ionization. Therefore, a high-energetic electron beam is guided through the center region of the EBIT where positively charged ions are trapped. The confinement is similar to Penning traps in which the radial confinement is done by a strong magnetic field, whereas the axial confinement is done by adjacent cylindrical electrodes (so-called drift tubes, Fig. 3.2) creating a radially symmetric electric field and by space-charge effects through the electron beam. For positively charged ions, the confinement is enhanced due to space charge effects by the electron beam crossing the trap region. The magnetic field can be generated by superconducting magnets (HD-EBIT) or permanent magnets (tt-EBIT). The latter allow operation in a non-cryogenic environment and a very compact design [59].

The electric drift tube potentials for the axial confinement form a potential well that allows the ions to leave the center either continuously via an energy gain from the electron beam (leaky mode) or in bunches (pulsed mode) by pulsing certain drift tube potentials.

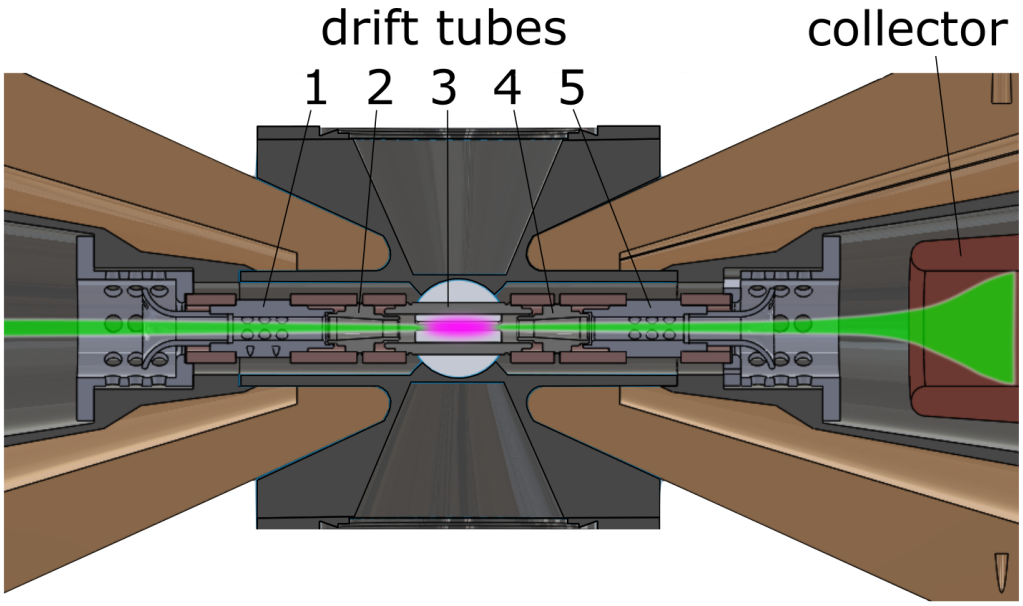

Figure 3.2: Cross-sectional view of the central region of the tt-EBIT in the CAD-model. The green beam and purple cloud represents a visualization of the electrons and the ions [60].

Inside the central trap region of the EBIT different physical processes take place which influence the extracted distribution and number of charge states [61]. The ions are created by electron-impact ionization. In this process, an electron with kinetic energy E_{kin} higher than the ionization potential P_{ij} is able to remove an electron from the j-th shell of the ion in charge state i. The total cross section σ for single ionization from charge state i to $i+1$ is given by a semi-empirical formula by Lotz [62]

$$\sigma_{i\to i+1}^{ioniz}(E_{\mathrm{kin}}) = \sum_{j=1} a_{ij} q_{ij} \frac{\ln\left(E_{\mathrm{kin}}/P_{ij}\right)}{E_{\mathrm{kin}} P_{ij}} \left\{1 - b_{ij} \exp\left[-c_{ij}\left(\frac{E_{\mathrm{kin}}}{P_{ij}} - 1\right)\right]\right\}, \tag{3.1}$$

where a_{ij}, b_{ij}, c_{ij} are empirical constants, q_{ij} is the number of electrons in the j-th shell where P_{i1} denotes the ionization potential of the outermost shell, P_{i2} of the next inner sub-shell, etc. Typically σ peaks at around $E_{\mathrm{kin}} \approx 3P_{ij}$ and decreases towards higher and lower E_{kin}. In case $E_{\mathrm{kin}} \gg P_{ij}$, (3.1) simplifies to:

$$\sigma_{i\to i+1}^{ioniz}(E_{\mathrm{kin}}) = \sum_{j=1} a_{ij} q_{ij} \frac{\ln\left(E_{\mathrm{kin}}/P_{ij}\right)}{E_{\mathrm{kin}} P_{ij}} \propto \frac{\ln E_{\mathrm{kin}}}{E_{\mathrm{kin}}}. \tag{3.2}$$

The effective rate of ionization for a charge state i with an ion density N_i is then given by

$$R_{i\to i+1}^{\text{ioniz}} = \frac{J_\text{e}}{e} N_i \sigma_{i\to i+1}^{\text{ioniz}}(E_\text{kin}) f(r_\text{e}, r_\text{i}), \tag{3.3}$$

where J_e is the electron-beam current density and $f(r_\text{e}, r_\text{i})$ is a factor taking into account the spatial overlap between the ion density distribution and the electron beam characterized by their radii r_e, r_i. The maximum kinetic energy of the electron beam is determined by the potential difference between the drift tube and the cathode at potential V_DT and V_c, respectively. Due to space-charge effects of the electron beam itself, the maximum kinetic energy is lowered, which is taken into account by the space charge potential V_SC:

$$E_\text{kin} = e\left(V_\text{DT} - V_\text{c} - V_\text{SC}\right). \tag{3.4}$$

Recombination processes counteract the ionization (ioniz) either by radiative recombination (recomb) with electrons or charge exchange (chgex) between ions. In addition, the ions are heated by the electron beam through Coulomb collisions. An equilibrium temperature is achieved by ion-ion energy exchange and evaporative cooling. In case ions with charge q have a kinetic energy greater than q times the trap potential V_trap, they can escape the electrostatic well potential of depth $V_\text{trap,rad}$ in radial (radesc) or of depth $V_\text{trap,ax}$ in axial direction (axesc) and are lost for any further charge breeding processes. The evolution of the ion densities N_i in a charge state i can then be described by a rate equation incorporating these processes:

$$\begin{aligned}\frac{\mathrm{d}N_i}{\mathrm{d}t} = R_{i-1\to i}^{\text{ioniz}} - R_{i\to i+1}^{\text{ioniz}} + R_{i+1\to i}^{\text{recomb}} - R_{i\to i-1}^{\text{recomb}} + R_{i+1\to i}^{\text{chgex}} \\ - R_{i\to i-1}^{\text{chgex}} - R_i^{\text{axesc}} - R_i^{\text{radesc}} + R_i^{\text{source}}.\end{aligned} \tag{3.5}$$

For a continuous injection of neutral gas

$$R_1^{\text{source}} = \frac{J_\text{e}}{e} N_0 \sigma_{0\to 1}^{\text{ioniz}} \tag{3.6}$$

and for $i > 1$,

$$R_i^{\text{source}} = 0. \tag{3.7}$$

The charge-state distribution depends on various operation parameters and has a specific temporal evolution approaching a steady state and thermal equilibrium. Based on the rate equations, the charge-state evolution can be calculated (Fig. 3.3).

The electron beam is provided by a thermionic emission source. In this emission source, a cathode is heated. In this way the thermal excited electrons inside the cathode material overcome the work function of the material and can leave the material. By applying a negative voltage (typically in the kV range), the electrons are repelled from the electrode and, by using additional electrodes, the electron beam can be shaped and focused. The achievable emission current, in case there is no limitation

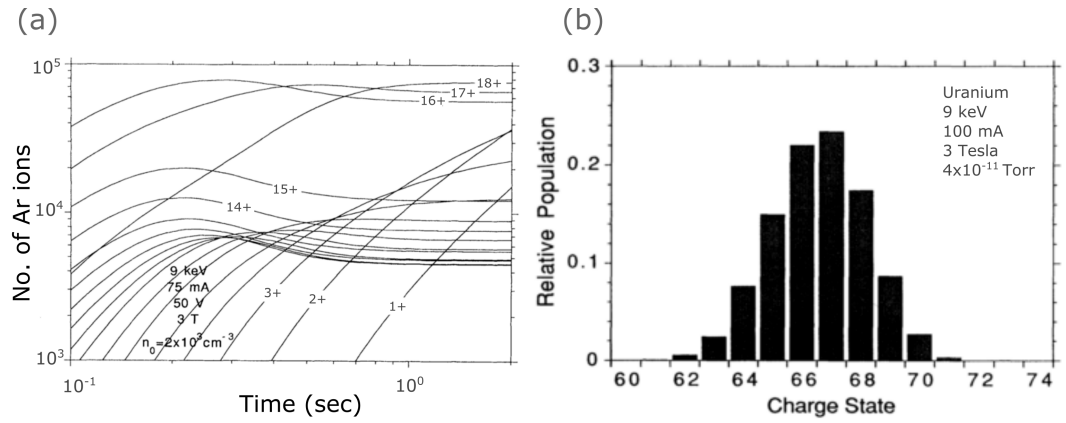

Figure 3.3: Exemplary calculated charge-state distributions: (a) temporal evolution of argon charge states [61] (b) calculated steady-state charge-state distributions for uranium [63].

due to space charge, is described by Schottky's law for field enhanced thermionic emission, where the emission current density J_e depends on the temperature of the cathode T_c, its work function W_c, the reduction of the work function by the applied electrical field ΔW and a material specific constant A_c [64]:

$$J_e(T_c, W_c) = A_c T_c^2 e^{-\frac{-(W-\Delta W)}{k_B T_c}}. \tag{3.8}$$

From (3.3) follows that a high electron current density J_e in the center region is favorable for reaching the highest charge state. The magnetic field forms a fringing field with a steep axial gradient towards the trap center forming a nonlinear lens and compresses the electron beam which increases the current density. Space-charge effects are a crucial limitation in the current densities for both the extraction of electrons from the emission cathode and for the compression of the beam. They can be calculated from Herrmann's Theory [65–67]. The maximum electron beam compression by a magnetic field is achieved for a perfect Brillouin flow, which is the maximum current density for a laminar flow of electrons in a magnetic field [68]. In this case, space charge and centrifugal forces acting on each electron are equal to the Lorentz force. The potential due to space charge effects V_{SC} is responsible for trapping the ions radially. Assuming the electron beam has a homogeneous charge distribution for a radius $r \leq r_0$, there is no space charge for $r > r_0$ and the drift tube

potential is $V_{DT} = 0\,\mathrm{V}$, then the V_{SC} can be calculated as [69]:

$$V_{SC}\,(r \leq r_0) = \frac{I_e}{4\pi\epsilon_0 v_z}\left[\left(\frac{r}{r_0}\right)^2 + \ln\left(\frac{r}{r_0}\right)^2 - 1\right], \tag{3.9}$$

$$V_{SC}\,(r \geq r_0) = \frac{I_e}{4\pi\epsilon_0 v_z}\ln\left(\frac{r}{r_{DT}}\right)^2. \tag{3.10}$$

r_{DT} is the radius of the inner drift tube, I_e is the electron beam current, ϵ_0 is the vacuum permittivity and v_z the electron velocity given by $v_z = \sqrt{\frac{2e(V_{DT}-V_c)}{m_e}}$. The electron beam radius r_0 can be estimated from the initial radius of the beam determined by the cathodes diameter and the compression by the ratio of the magnetic fields at the cathode and in the center region [70]. For the tt-EBIT parameters used in this thesis, the space charge potential in the center of the EBIT is in the order of $-9\,\mathrm{V}$ (Fig. 3.4).

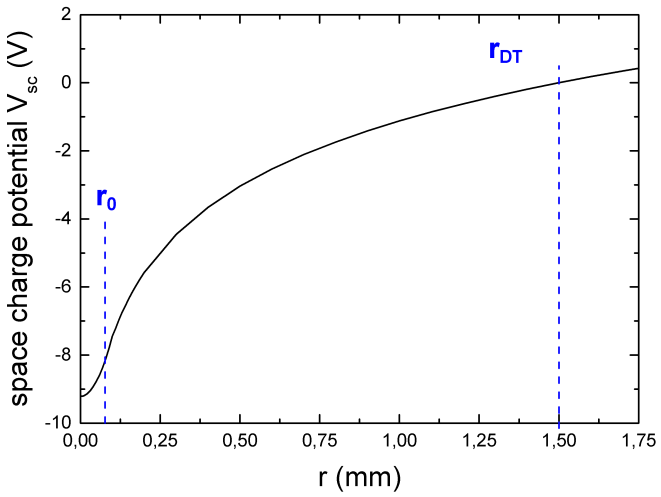

Figure 3.4: Predicted space charge potential V_{SC} as a function of the radius in drift tube 3. As typical parameters for the tt-EBIT, $r_0 = 88\,\mu\mathrm{m}$, $V_{DT} - V_c = 3\,\mathrm{kV}$, $I_e = 5\,\mathrm{mA}$ and $r_{DT3} = 1.5\,\mathrm{mm}$ are used.

3.3 Wien filter

Both the continuous and the pulsed extraction from an EBIT yield a distribution of many different charge states at the same time. However, the main aim is to inject a single ion species with a specific charge state into the Penning trap. Therefore, the ion beam must be separated according to its charge-to-mass ratio q/m. To achieve this, either a separator magnet (this will be later on used for the ions from the

HD-EBIT) or a Wien filter (positioned behind the exit of the tt-EBIT) can be used. A detailed characterization of the Wien filter (Colutron Research Cooperation, model 600-B [71]) was done previously [72].

3.4 Microchannel plate detector

For the detection of the ions at strategic positions along the beamline, various detection units are installed (Fig. 3.1). Each of these units contains a microchannel plate detector [73] (Photonis USA, Inc., model APD 2 PS 18/12/10/5 I 40:1 P43 [74]). An MCP is an array of multiple single electron multipliers parallel to one another. These are made of channels with a high aspect ratio[2], with a coating on the inside walls enhancing the secondary electron emission upon ion impact. To mimic a dynode-like behavior, a voltage is applied across the front and back side accelerating the secondary electrons to create an avalanche of electrons (Fig. 3.5). The axis of the channels is slightly tilted against the entrance axis of the ions and two MCP plates are stacked on top of each other, forming a so called chevron configuration. These electrons are again accelerated towards the phosphor screen where they are converted to photons in the visible spectral range, detectable for a CCD camera. This allows a visual mapping of the ion beam position and shape (Fig. 3.6). The detection units are installed on linear manipulator stages mounted in a CF160 double cross so they can be moved in the pathway of the ions if necessary. Through a view port and a mirror, optical access for a CCD camera (Allied Vision Technologies, model Prosilica GC 655 [75]) is provided.

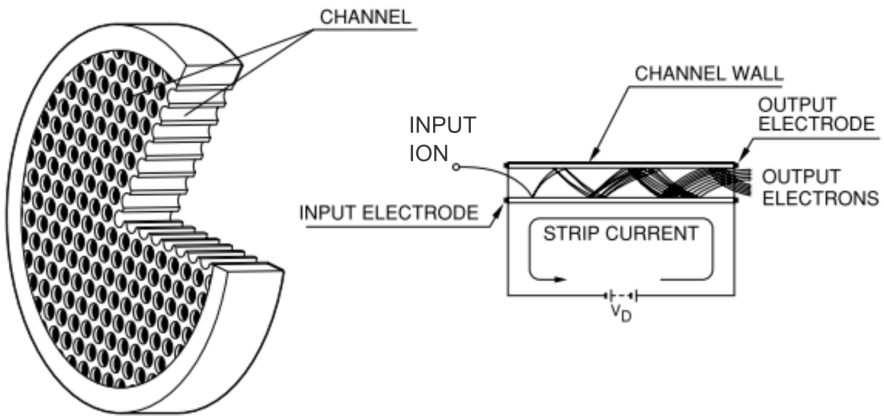

Figure 3.5: Schematic structure of a microchannel plate [76].

[2]Typically between 40 and 100 and diameters are in the range of 10 µm to 100 µm

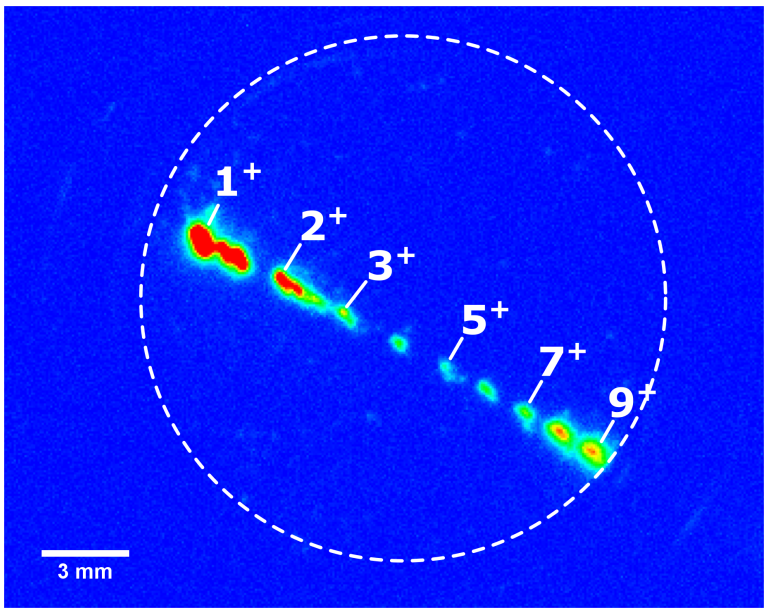

Figure 3.6: Exemplary image of a sequence of $^{40}Ar^{1+}$ to $^{40}Ar^{9+}$-ions mapped on an MCP positioned behind the Wien filter operated in low dispersion. The signal of ambient rest gas ions is superimposed on the lowest charge states. The dotted circle denotes the active area of the MCP with a diameter of 18 mm.

3.5 Pulsed drift tube

The ions extracted from the Heidelberg EBIT have a transfer kinetic energy $qU_{transfer}$ of typically about $q \times 10\,kV$ [52]. The maximum voltage which can be applied to the capture electrodes of the Penning-trap system is about $\pm 500\,V$. Therefore the ions have to be slowed down to a remaining kinetic energy of about $\lesssim 200\,qV$, which allows a dynamic capture of the ions in the Penning trap. The maximal kinetic energy for which a dynamic capture in the Penning trap is possible is given by the maximum potential that can be applied to the electrodes of the Penning trap. This potential is limited the dielectric strength of the Penning-trap electrodes which are separated from each other by only 140 µm. The deceleration in the pulsed drift tube uses an approach similar to an in-trap lift electrode [77]. When the ions enter the drift tube, the potential of this electrode is on a "high" potential U_{lift} slightly below the ions transfer potential $U_{transfer}$. While the ions enter this drift tube, their kinetic energy is reduced by the gained potential energy qU_{lift}. Once the ions have entered the drift tube, the lift electrode is switched to ground potential and reducing the ions potential while leaving their kinetic energy unaffected. When the ions leave the lift electrode section, they have now the remaining kinetic energy of $q\,(U_{transfer} - U_{lift})$.

3.6 Cryostat and magnet

The Penning-trap system will operate at liquid-helium temperature of about 4.2 K. The magnet was previously used for high-precision mass measurements at the SMILETRAP experiment in Stockholm [78]. It is a superconducting magnet (Oxford Instruments, NMR Division, Type 200/130 Cryostat Family Type [79]) with a vertical room temperature bore (130 mm inner diameter) and is charged to a maximum central field strength of about 4.02 T. Since the Penning-trap system and the detection electronics have to be kept at cryogenic temperatures, a cryostat system was developed (Fig. 3.7). The experimental setup consists of two dewar vessels and the trap chamber which is inserted into the bore of the magnet[3]. The trap chamber and the cryogenic electronic[4] section are thermally coupled to a liquid-helium dewar that acts as a cryogenic heat sink. The liquid-helium dewar itself is then embedded in a liquid-nitrogen stage at 77 K. For the design of this cryostat, it is crucial to achieve a high thermal decoupling between elements at different temperatures in order to minimize the heat flux into the cryogenic section. To reduce the heat transfer through convection, the whole system is kept at an insulation vacuum $\leq 1 \times 10^{-4}$ mbar. The transfer by thermal radiation is reduced with multi-layer insulation (MLI). Therefore the nitrogen vessel and other thermoconductive structural elements are covered by stacks of 10 to 40 layers of low emissivity polyester foil aluminized on both sides and separated by a layer of scrim, acting as almost floating radiation shields. In order to reduce the heat flow by thermal conduction, the support and suspension structures, should feature both low thermal conductivity and high mechanical stability at the same time. Therefore the support structures holding the liquid nitrogen vessel are hollow stainless steel rods, whereas the liquid helium cryostat including the trap chamber is suspended on vespel® rods [80].

[3] PhD Thesis I. Arapoglou, in preparation
[4] PhD thesis A. Weigel, in preparation

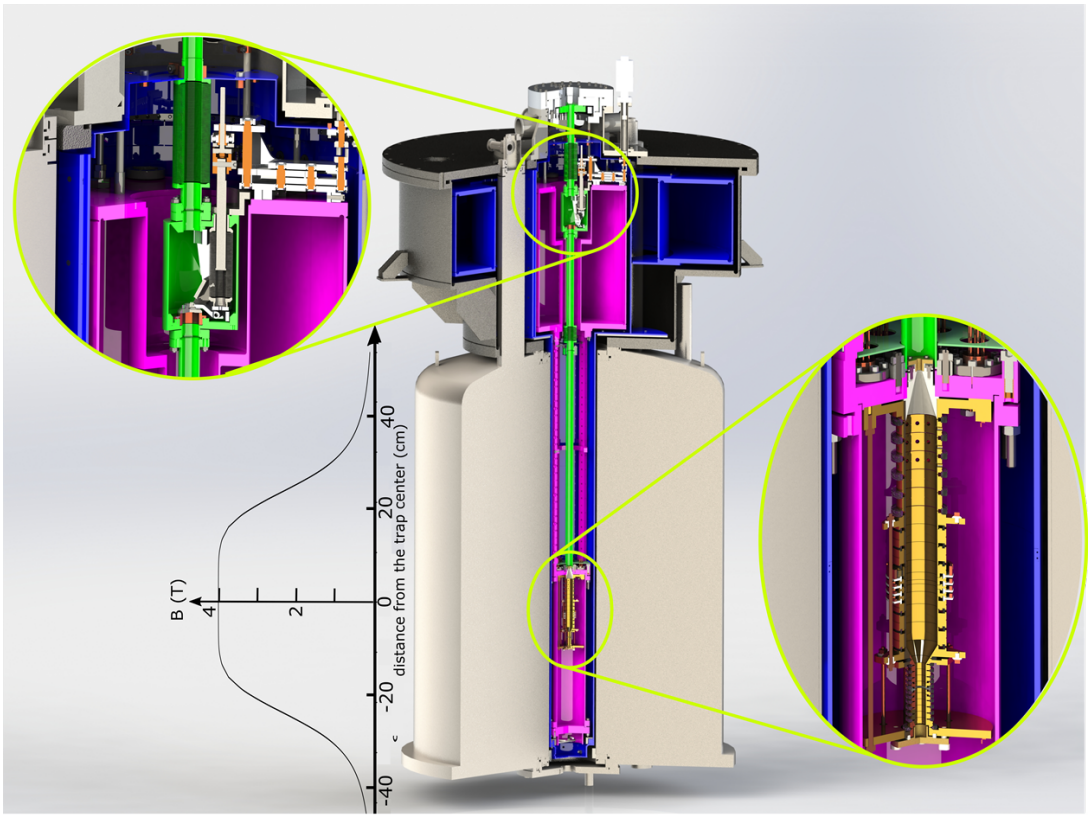

Figure 3.7: Cross sectional view of the ALPHATRAP magnet and cryostat. The 77 K section is highlighted in blue and the 4.2 K section in magenta. The blue and magenta vessels on top contain the liquid nitrogen (54 L) and helium (15 L), respectively. In the center of the magnet bore, the beamline (left inset shows the cryovalve) ends at the Penning-trap system (right inset), which is encapsulated by the trap chamber at 4.2 K and the copper tube of the 77 K section.

3.7 Double Penning-trap system

3.7.1 The double-trap setup

The design and principle of the Penning-trap system is based on previous systems already successfully used in the Mainz g-factor experiment [3–5], where it was developed [48]. Today, this approach is well established and used in high-precision Penning-trap experiments [81]. It consists of two orthogonal and compensated open-endcap, cylindrical Penning traps [40] (Fig. 3.8). The trap tower is made of gold-plated OFHC[5] copper electrodes for the 5 electrode analysis trap (AT), 7 electrode precision trap (PT) and for the ion capture, transport and storage section. The AT contains the magnetic bottle and serves solely for the detection of the spin states. The precise measurement of the free cyclotron frequency and the sampling of the Larmor resonance is done in the PT. The spatial separation is necessary to reduce the magnetic field inhomogeneities in the PT caused by the magnetic bottle in the AT, which lead to an energy depend modification and frequency shift of the cyclotron and magnetron mode. The traps are installed in the homogeneous magnetic field in the center of the superconducting magnet (Fig. 3.7). The inner diameter of the AT and PT electrodes are 6 mm and 18 mm, respectively, with an absolute precision better than 10 µm on the length and diameter of the electrodes. The PT is positioned in the most homogeneous area of magnetic field for the precise measurement of the motional eigenfrequencies and spin flip induction. In addition a magnetic bottle is superimposed to the AT (Fig. 2.6 (a)), which allows a spin state detection by exploiting the continuous Stern-Gerlach effect (section 2.3.2). The magnetic field inhomogeneity is created by replacing a regular ring electrode of the AT with a ferromagnetic CoFe ring electrode (Fig. 2.6 (a)). The strength of the magnetic bottle characterized by its B_2 term depends both on the ring geometry[6] and the saturation magnetization M_S of the used material. The CoFe alloy (Vacuumschmelze, VACOFLUX®50 [82]) used for the ring has a saturation magnetization of $M_S^{CoFe} \approx 2.35\,\mathrm{T}$. This creates a B_2 field inhomogeneity of about $45\,\mathrm{mT/mm^2}$. This value is derived from simulations and can be measured experimentally by a position-dependent measurement of the magnetic field strength.

3.7.2 Measurement procedure in a double-trap system

As shown in equation (2.36), the g-factor can be determined by measuring the frequency ratio $\Gamma_0 = \frac{\omega_L}{\omega_c}$. Therefore the spin state is first determined in the AT by using the continuous Stern-Gerlach effect in the inhomogeneous magnetic field of

[5] Oxygen-free high thermal conductivity

[6] Higher values for B_2 could be reached for smaller trap diameter. The diameter is limited since the trap acts also as a waveguide for the microwave radiation inducing the spin flips. Therefore, the size of the trap is restricted depending on the microwave wavelength.

the magnetic bottle. Then, the ion is adiabatically[7] transported to the PT, where ω_c is measured in the homogeneous magnetic field. At the same time[8], one tries to induce a spin flip via irradiation of a low power microwave signal with frequency ν_{rf}. Subsequently, the ion is adiabatically transported back to the AT, where the spin state orientation is again analyzed in the magnetic bottle (Fig. 3.9 (a)). By repeating this several times for different ν_{rf}, the spin flip probability as function of Γ_0 can be obtained (Fig. 3.9 (b)) and a value for the g-factor can be extracted by using (2.36). In this measurement scheme, the precise determination of ω_c and ω_L is done in the homogeneous field of the PT, whereas the spin state analysis is done in the AT, yielding a spatial separation of these measurements. The spatial separation of the homogeneous and inhomogeneous magnetic field is one of the main advantages of this double-trap technique.

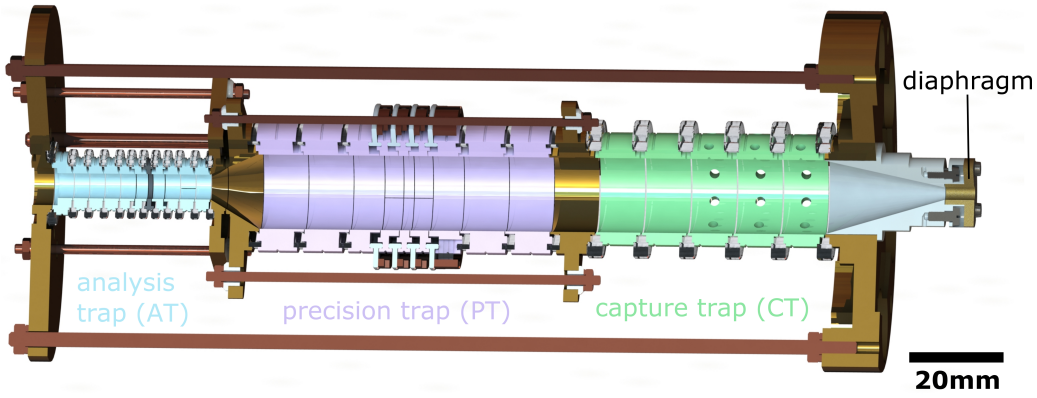

Figure 3.8: Cross-sectional view of the Penning-trap system as a CAD-model.

3.8 In-trap ion source

During the assembly of the experiment the decision was made to equip the trap system with an additional ion source attached to the trap tower. This has two advantages: On the one hand it allows to test, commission and debug the Penning-trap system independently of the operability of the external components, for instance the injection from the room temperature beamline via the tt-EBIT. On the other hand, it provides an easy to operate and reliable device for the in-trap production of singly charged beryllium ions $^9Be^+$. In turn, these $^9Be^+$ ions can be used in a planned implementation of sympathetic laser cooling of HCI in the Penning trap.

[7] Adiabatic means here, that the variation of the motional amplitudes is comparably slow with respect to the eigenfrequencies. In the best case, this transport does not change the energy or spin state.

[8] As a consequence of ω_L and ω_c being measured simultaneously the ratio Γ_0 is self-consistent and does not depend on the magnetic field drift between subsequent measurements

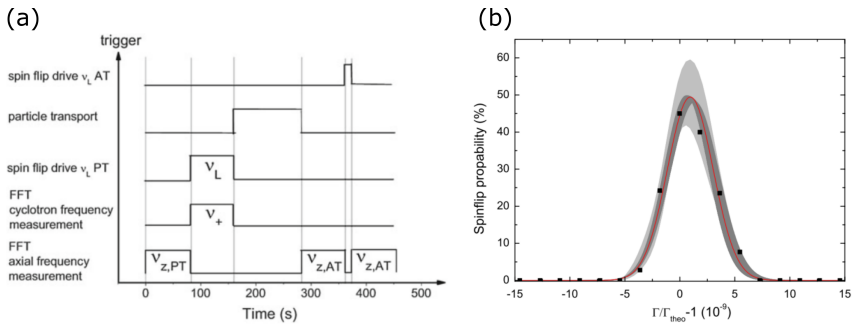

Figure 3.9: (a) Principal measuring sequence for a g-factor determination via the double-trap technique. The ν_L measurement is sandwiched by two ν_z measurements in order to cancel first order voltage drifts. This sequence is repeated several hundred times and for different spin flip drive frequencies ν_{rf} (b) Spinflip probability as function of the ratio $\Gamma_0 = \frac{\omega_L}{\omega_c}$. The dark grey band indicates the confidence band of the Gaussian fit by using the maximum-likelihood method. The light grey area indicates the 1σ-prediction band for the measurement data distribution. The exemplary data are taken from [5] and similar resonances are expected to be measured in the ALPHATRAP experiment.

The source is very similar to the one used in the Mainz g-factor experiments [3–5] as a "creation trap" for an in-trap production of HCI up to lithium-like[9] $^{40}Ca^{17+}$ [22]. Ions are created by electron-impact ionization through an electron beam. Fig. 3.10 (a) shows a sketch of the in-trap ion source, which consists of a field emission point (FEP), an acceleration electrode and an anode. The tip for the FEP is made by electrochemical etching of a tungsten wire, where the very end of the tip is only the size of a few to one atom of the wire material, similar to tips used for scanning tunneling microscopes. The extraction of electrons from this cold cathode is based on the principle of field emission by high electric fields. For electrons with an energy lower than the work function of the material, it is possible to tunnel through this barrier as described by the Fowler-Nordheim theory [83]. To enable this tunneling, a strong electric field at the tip of the FEP has to be created. This can be done by setting the acceleration electrode to a high positive potential in the range of a few 100 V, while keeping the FEP cathode on a negative potential. Now, this electric field deforms the potential barrier at the interface of the tip material and the vacuum. As a consequence of this deformation, the probability for electrons to tunnel through this barrier is increased, and electron emission can take place. The cathode potential from which the electron start defines their kinetic energy. The necessary kinetic energy depends on the ionization potential for the charge state

[9] The ionization potential of $^{40}Ca^{17+}$ is ≈1.2 keV [30].

of the ion which is supposed to be created. In the case of the production of $^{9}Be^{+}$ ions[10], a negative potential of about −30 V is sufficient. The generated electron beam is then accelerated and guided through a hole (diameter of 0.7 mm) in the anode into the Penning trap. There, one ring electrode is put to higher negative potential and the electrons are reflected back towards the FEP. The electrons follow hereby the strong homogeneous magnetic field lines. By keeping the emission of the FEP continuously turned on, the current density of this electron beam builds up while the beam is reflected back and forth. Through space charge effects the beam widens in diameter until the electrons starts to impinge on the anode where atoms are evaporated upon the electron impact and subsequently ionized in the electron beam. For the production of different ion species, the corresponding material has to be placed around the hole in the anode. This can be done by depositing a thin layer of the material on the anode or by attaching a foil in which a small hole is pricked out onto the anode. In the case of the production of $^{9}Be^{+}$ ions, a beryllium or copper beryllium foil can be attached on a second identical anode. The whole FEP ion source is attached to lower end of the Penning-trap tower below the AT[11] (Fig. 3.10).

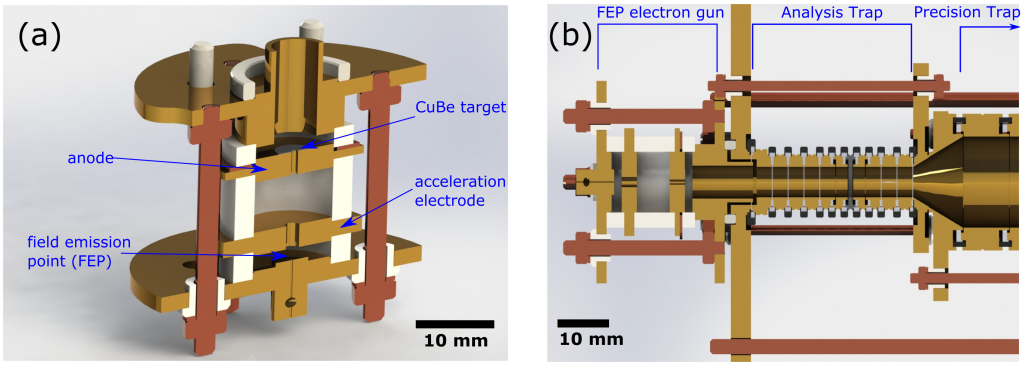

Figure 3.10: (a) Cross sectional view of the FEP ion source design. (b) The ion source mounted below the AT.

[10] The first ionization potential for $^{9}Be^{+}$ is 9.32 eV [84].

[11] Note that this configuration will be used temporarily at the initial commissioning phase of the ALPHATRAP experiment. Later on the rf waveguide for inducing spin flips will be connected at this position.

4 Results

The aim of this work was to set up and commission the ALPHATRAP beamline and to demonstrate the efficient ion transport. At the beginning of the work, in May 2015, the beamline was assembled, and it was possible to operate it in an offline mode in a separate laboratory. At this time, the later on vertical part of the beamline was mounted horizontally. The setup except for minor modifications was similar to the one shown in Fig. 3.1. The beamline section after the second quadrupole bender is the later on vertical part of the beamline connecting the ion sources (tt-EBIT and Heidelberg EBIT) located on the ground floor with the cryostat and magnet located in the basement.

The motivation to build up the system in an offline laboratory was to be able to test each component individually, so it would be easier to change, modify or repair malfunctioning parts, before the beamline is finally assembled in the experimental hall with restricted access since it is a radiation safety area. While the characterization and demonstration of the Wien filter and ion optics were shown in previous theses [72, 85], a transport of ions from the tt-EBIT through the whole beamline was not yet shown. The results presented in this chapter focus on the characterization of the tt-EBIT and a demonstration of the ion transport. The tt-EBIT is a prototype EBIT and developed in the group of PD Dr. José Crespo at the Max-Planck-Institut für Kernphysik. One of the results of this work is the production of argon ions up to $^{40}Ar^{16+}$, which were extracted in bunches from the tt-EBIT. The transport of bunched argon ions to the end of the beamline was shown for the first time. For the deceleration of the ions by the pulsed drift tube, time-of-flight (ToF) measurements are presented. The experimental setup used to obtain these results is shown in Fig. 4.1.

In the following, abbreviations for different experimental parameters will be used: The voltages applied to the drift tubes and extractor electrode of the tt-EBIT are denoted as $V_{\mathrm{DT,i}}$ and V_{extr}, where the index i represents the drift tubes 1 to 5. Drift tube 1 is oriented towards the beamline and drift tube 5 faces the electron gun. The potentials of the cathode, focus and anode of the electron gun are denoted as $V_{\mathrm{c}}, V_{\mathrm{f}}$ and V_{a}. The emission current of the cathode is called I_{e} and the current applied to the Wien filter is called I_{WF}.

Due to a technical malfunction which broke the cathode, the tt-EBIT was unfortunately not available anymore for the second half of this thesis. Nevertheless useful results were obtained in the offline mode which will serve as starting point for the upcoming final commissioning of the beamline at its final position (Fig. 4.2). This results from tests in the offline laboratory will be presented in the following chapter.

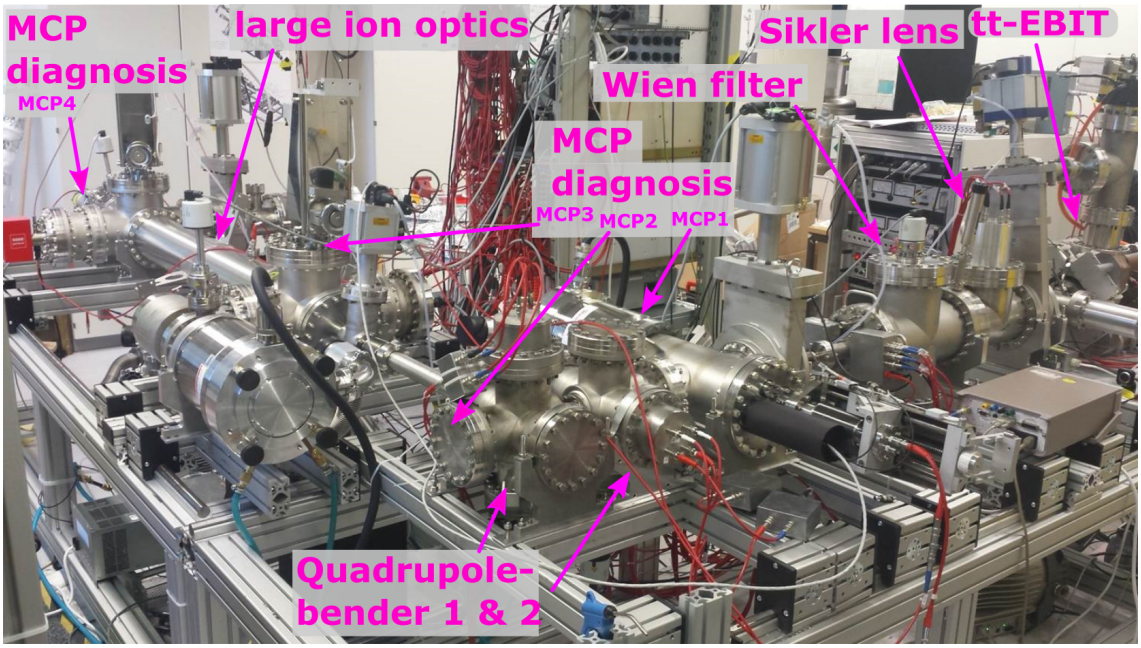

Figure 4.1: Photograph of the beamline in the offline laboratory. The most important components are labeled.

4.1 tt-EBIT characterization

The aim was to become familiar with the tt-EBIT, to know its strength and issues in order to find the best operation parameters for the upcoming commissioning and operation of the ALPHATRAP experiment. The measurements focus on the influences of different parameters on the extracted ions. Design and typical operation parameters of the used tt-EBIT can be found in Tab. 4.1 and in [32, 69].

Table 4.1: Typical parameters of operation for the tt-EBIT used for this thesis.

dimensions[1]	≈32 cm × 32 cm × 32 cm	V_{DT}[3]	1.5 kV to 1.7 kV
weight[1]	≈50 kg	V_c	≈ − 1.5 kV
rest gas pressure[2]	$<1 \times 10^{-9}$ mbar	V_f	−1.3 kV to −1.7 kV
B_{max}	0.74 T	I_e[4]	≈5 mA

[1] without vacuum pumps or electron beam source
[2] measured approx. 30 cm from the central region
[3] settings for subsequent measurements, values of most stable operation
[4] for the initially used BaO dispenser cathode

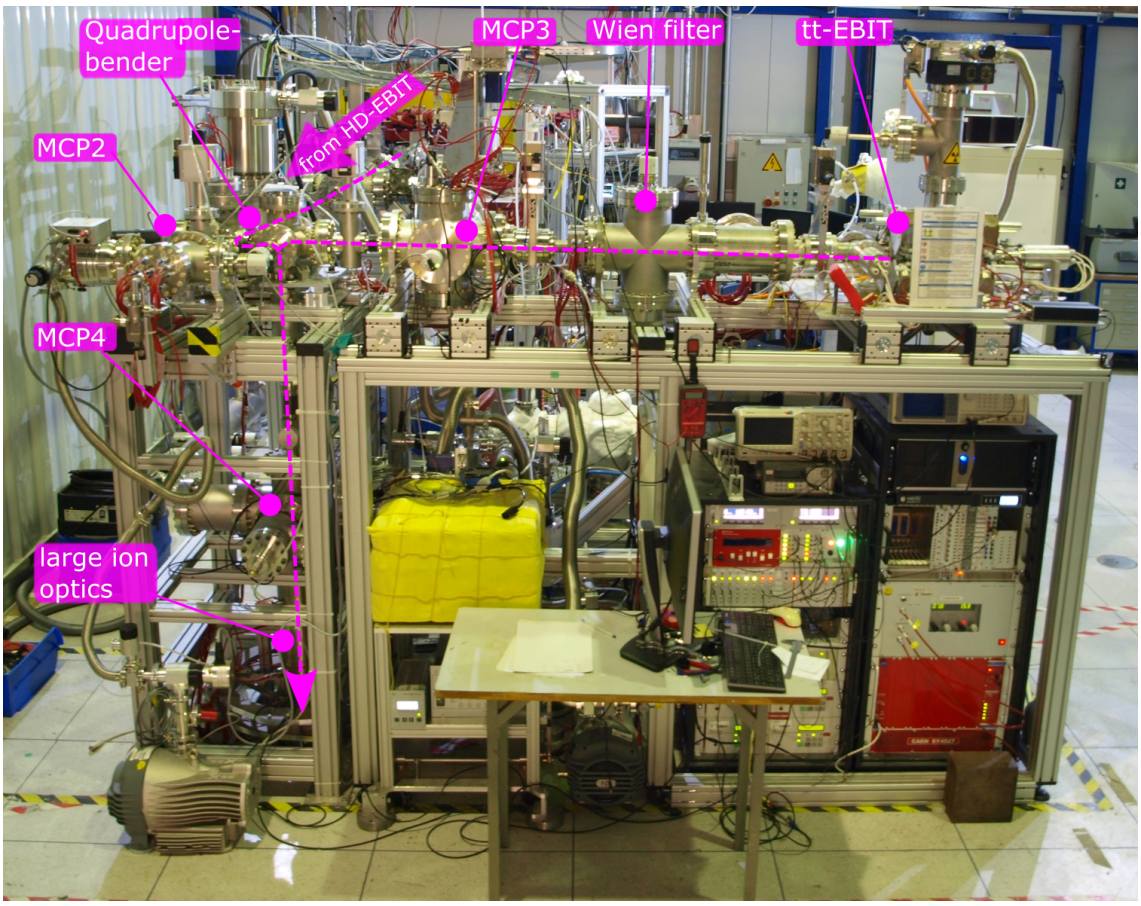

Figure 4.2: Photograph of the tt-EBIT and the room temperature beamline next to the HD-EBIT. The pathway of the ions coming from the tt-EBIT and HD-EBIT is indicated by a dotted line.

Data acquisition procedure

For measurements the drift tube and extractor electrode potentials were optimized, and the ions were ejected. After leaving the tt-EBIT, the ions pass a Sikler lens [86] and are focused into the Wien filter. The Wien filter spatially separates the bunched ions according to their charge-to-mass ratio, and the ions hit the MCP with a phosphor screen behind. Images of the the phospor screen can be taken with a CCD camera to record the intensity profile and position of the ion beam. For this separation the magnetic field in the Wien filter is kept constant, while the electric field is varied. While scanning the Wien filter deflection voltage, for each voltage step images of the phosphor screen are taken (Fig. 4.3 (a)). Since the Wien filter voltage is increased in each step, the charge states move in the plane of dispersion. By projecting each acquired image into the plane of dispersion of the Wien filter (see Fig. 3.6), individual line profiles are obtained (Fig. 4.3 (b)). These line profiles are stitched together (Fig. 4.3 (c)) and a projection along the tilted line of dispersion yields a spectrum of

the charges-state distribution (Fig. 4.3 (d)).

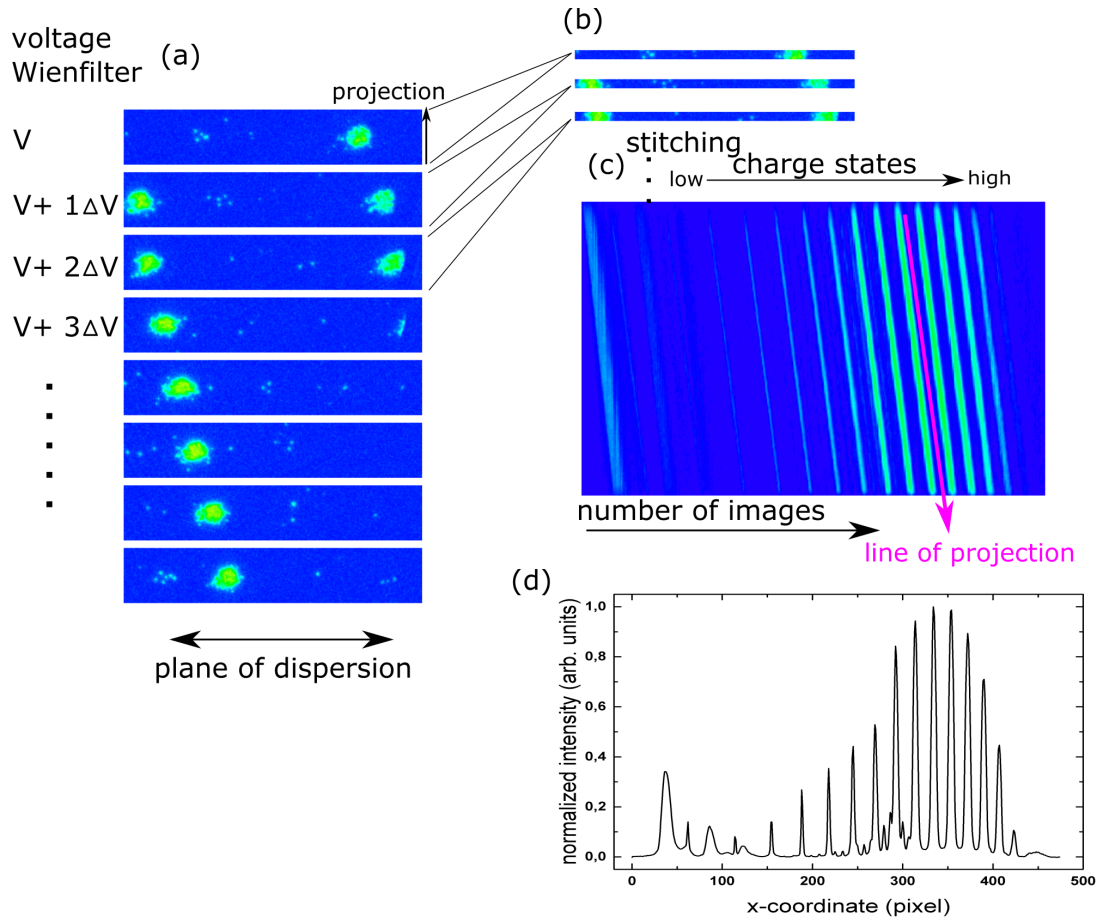

Figure 4.3: Exemplary scheme for stitching the taken images to obtain the charge-state spectra. Explanation see text.

The voltages on the MCP and phosphor screen as well as the CCD-camera gain and exposure time are chosen such, that the most intense ion charge states are unsaturated in the acquired CCD image. If measurements are not done one after another in a short time or with the same settings, attention should be paid when comparing the signal intensities or count rates shown in different figures even though all attempts were made to keep all settings the same and reproducible. One reason for fluctuations within this thesis is found in the fact that for different measurements the MCP detector model differs due to reconstruction of the whole beamline or due to the fact that the measurements were done at different diagnosis unit downstream the beamline (e.g. MCP1 and MCP4). Depending on which MCP was used and which bias voltage was applied across the MCP plates, the gain of the MCP can differ by more than an order of magnitude [73].

Pulsed mode

The ions are extracted in bunches from the tt-EBIT, which is operated such that the voltage configuration on the drift tubes forms an axially confining minimum in the center of the trap region. Drift tube 3 has the lowest potential and therefore a potential minimum along the length of drift tube 3 is established. In this potential well, the ions are trapped and ionized by the electron beam crossing this volume. The longer the trap is set to this confining configuration, the higher the charge states that are bred until a certain equilibrium is reached depending on different parameters [61] (Fig. 3.3), as discussed in section 3.2. After this breeding time, the potential on the center drift tube is switched (switching time ≈100 ns) to a value higher than the adjacent drift tubes. In this configuration the ions are ejected out of the tt-EBIT. The time for the center electrode being on this high-potential configuration will herein be called ejection time. For the injection of the ions into the Penning-trap setup, the ions have to be bunched for enabling a dynamic capture. This requires a precise timing of switching the ejection, deceleration (section 4.2) and capture potentials. For this reason, a small width of the ToF distribution is crucial. A small width in the ToF distribution reduces the loss of ions in the deceleration and capture process and hence keeps the transmission and transport efficiency of the whole beamline system and the capturing efficiency of the Penning-trap system high. The width of the ToF is among other factors determined by the tt-EBIT drift tube geometry, ejection potentials and the initial energy spread of the ion bunch.

Influence of the electron kinetic energy E_{kin}

In this measurement series, the influence of the electron kinetic energy on the charge-state distribution was investigated. As explained in section 3.2, the ionization cross section for ions by electron impact depends on the kinetic energy of the electrons, E_{kin} (3.1), which is mainly given by the drift tube and cathode potentials (3.4). By changing these two potentials, the kinetic energy of the electrons in the central drift tube was varied in the range from 2923 eV to 3405 eV. As can be seen from Tab. 4.2, it is not possible to create ions in charge state $i > 16$, since the therefore required ionization potential P_{i1} is strongly increased due to the 1s-shell closure and $P_{17,1}$ is larger than E_{kin}.

Table 4.2: Ionization energies P_{i1} in keV for argon [30].

i	1	3	5	7	9	11	13	15	16	17	18
P_{i1}	0.01	0.04	0.07	0.12	0.42	0.54	0.68	0.86	0.91	4.12	4.42

Even though the electron kinetic energy is approximately three times the ionization potential $P_{16,1}$ for $^{40}Ar^{16+}$ and a maximum in the ionization cross section would be

expected, equation (3.5) shows that this does not imply a maximum in the abundance of this specific charge state. The breeding of the charge states in the center region is also governed by axial and radial escape rates, radiative recombination and charge exchange processes that differ significantly for different charge states. Therefore the maximum of the charge-state distribution lies below the charge state with the maximum ionization cross section [61].

The spectra were obtained for a charge breeding time of 333 ms and an ejection time of 20 µs, respectively. The Wien filter voltages and current were in the range of 50 V to 270 V and 1.5 A, respectively, corresponding to a nominal magnetic field of 32.1 mT [72] and the pressure was 2.2×10^{-9} mbar. The individual electrode potentials are listed in Tab. 4.3.

Table 4.3: Drift tube 3 is pulsed between the low value for breeding and the high value for ejection. The drift tube and cathode potentials were varied to obtain different kinetic energies of the electrons.

E_{kin}(eV)	V_{DT1} (V)	V_{DT2} (V)	V_{DT3} (V)	V_{DT4} (V)	V_{DT5} (V)	V_{extr} (V)	V_c (V)	V_f (V)	I_e(mA)
2923	1595	1600	1550/2044	1850	1750	93	-1373	-1309	-4.7
2976	1595	1600	1550/2044	1850	1750	93	-1426	-1493	-5.2
3091	1648	1656	1665/2330	1944	1946	250	-1426	-1493	-5.2
3405	1648	1656	1665/2330	1944	1946	250	-1740	-1666	-6.3

In agreement with the theoretical predictions and expectations, higher electron kinetic energies shift the maximum of the spectra towards higher charge states. For the last measurement at $E_{kin} = 3405$ eV, the cathode potential was increased from -1426 V to -1740 V, leading to an increase in the emission current I_e from -5.2 mA to -6.3 mA (Tab. 4.3). It was observed that this emission current decreased by $\approx$2 mA over 18 hours, whereas for higher cathode potentials the current remained constant. After changing the cathode potential to the higher initial value the emission current was even lower than before at this potential. The emission current slowly recovered in a couple of days, which was interpreted as a degeneration effect in the cathode, possibly after bombardment off the cathode surface with rest gas ions. Therefore, the emission current and cathode potential were kept at the lower value. Nevertheless, it was shown that with the current setup of the tt-EBIT the boron- and lithium-like argon ions $^{40}Ar^{13+}$ and $^{40}Ar^{15+}$ can be created.

Influence of the pressure

Furthermore, the influence of the argon injection pressure was investigated. Without any gas injection, the rest gas pressure was in the range from 6×10^{-10} mbar to 9×10^{-10} mbar. As seen from the previous measurement series, the charge-state

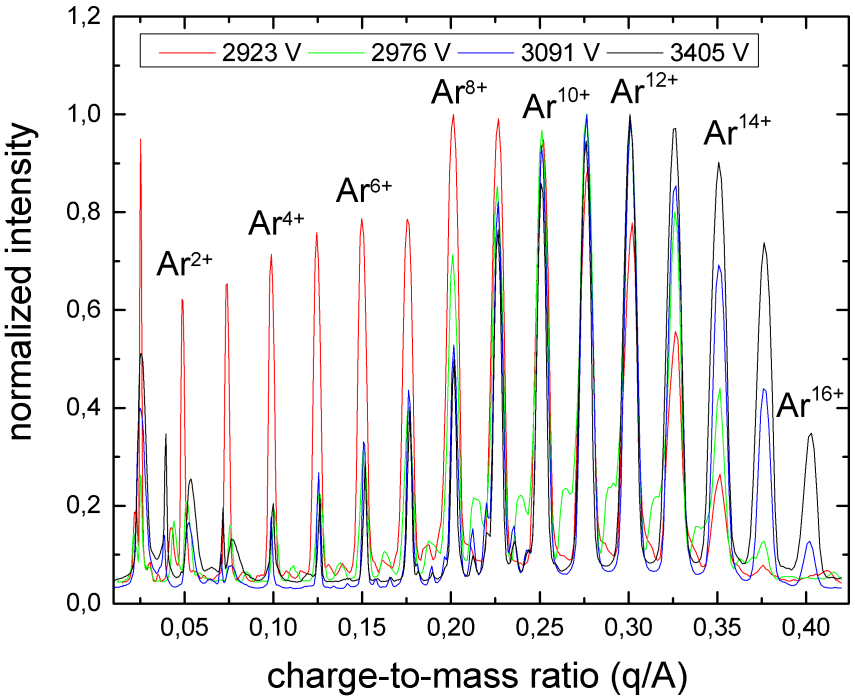

Figure 4.4: Argon extraction spectra obtained in the pulsed mode of the tt-EBIT and for different electron kinetic energies. The intensities are normalized to the maximum intensity of each charge-state distribution.

distribution does not solely depend on the ionization cross sections and kinetic energy of the electrons. Indeed, the interaction between the trapped ions also influences quite dominantly the obtained spectra, see equation (3.3). This motivated the following measurements in which it was examined how the injection pressure of the argon gas affects the charge-state distribution. A low injection gas pressure corresponds to a low density of neutral atoms inside the tt-EBIT trap chamber region which should reduce the rate of charge exchange and recombination processes. The following figures show how the charge-state distributions change for different pressures. The spectra were acquired with identical settings for the tt-EBIT, beamline and Wien filter (Tab. 4.4) as well as the detection with the MCP and CCD camera. Solely the pressure was increased incrementally from 1.0×10^{-9} mbar to 8.1×10^{-9} mbar, measured approximately 30 cm above the center region of the tt-EBIT (Fig. 4.5).

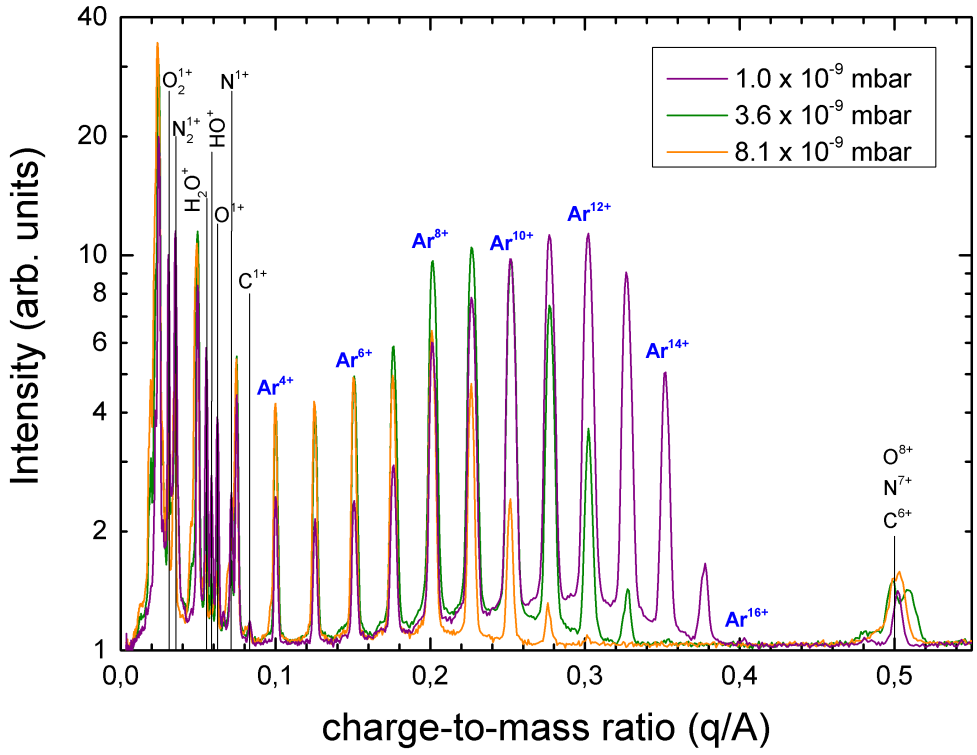

Figure 4.5: Charge-state distributions for different injection pressures of the Argon gas.

When turning off the argon injection, a spectrum of the ambient rest gas can be measured (Fig. 4.6). As expected, the rest gas spectrum has the composition of the ambient air. It consists mainly of oxygen from singly charged to fully ionized ions[1], respectively. The measurement without Argon injection was done in the end which explains the remaining argon ions in the rest gas spectrum. Nevertheless, it shows that the maximum of the argon charge-state distribution is shifted from $^{40}Ar^{12+}$ at 1×10^{-9} mbar to $^{40}Ar^{8+}$ at 8.1×10^{-9} mbar, and the total yield of ions is decreased at the same time.

The electron kinetic energy in this measurement was 2.8 keV and comparing this to the 2.9 keV in Fig. 4.4 (the pressure there was 2.2×10^{-9} mbar) the reduction of the pressure by a factor of 2 shifts the maximum of the distribution by almost 4 charge states from $^{40}Ar^{8+}$ to $^{40}Ar^{12+}$. Even though the potential configuration does not create a potential minimum at position of drift tube 3, a shallow trap is formed at drift tube 2 in which the ions could be trapped and bred. The signal was optimized to obtain the maximum signal for the ion distribution on the MCP. Even by forming a

[1] The ionization potentials for complete ionization of carbon, nitrogen and oxygen are 0.49 keV, 0.67 keV and 0.87 keV

similar shallow trap with drift tube 3, the obtained signal was worse. Therefore, on purpose the potential minimum was set for drift tube 2 to form a trap there.

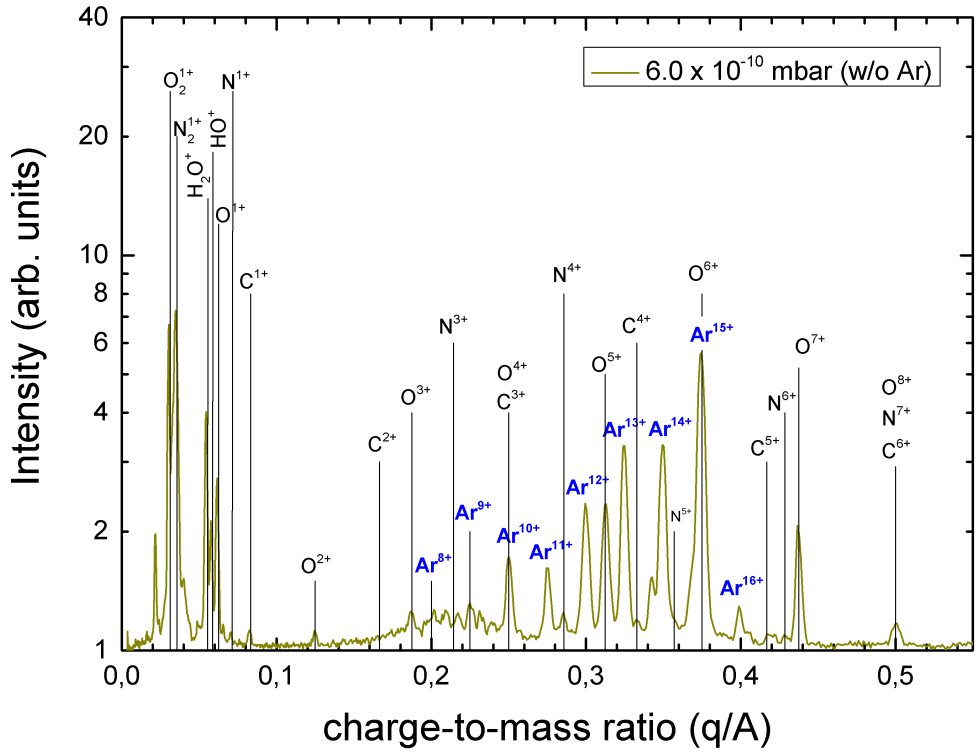

Figure 4.6: Charge-state distributions of the ambient rest gas in the tt-EBIT center region.

Table 4.4: Drift tube 3 pulsed between the low value for breeding and the high value for ejection. The pressure was varied from 0.6×10^{-9} mbar to 8.1×10^{-9} mbar.

V_{DT1} (V)	1594	V_{extr} (V)	343	I_e (mA)	-4.1
V_{DT2} (V)	1591	V_f (V)	-1121	breeding time (s)	2
V_{DT3} (V)	1637/2144	V_c (V)	-1183	ejection time (µs)	10
V_{DT4} (V)	1814	V_a (V)	110	I_{WF}	1.5
V_{DT5} (V)	1659				

Influence of the breeding time

The model for the charge-state evolution based on rate equations (3.5) shows that for long breeding times the dynamics slow down and approach a steady state condition (Fig. 3.3). Hence in these measurements the temporal evolution of the charge-state distribution will be investigated. For this purpose the acquisition method was changed. Instead of the CCD camera, a multichannel scaler (Stanford Research Systems, model SR430 [87]) was employed. This device uses an adjustable leading-edge discriminator and a fast counter with a minimal bin width of 5 ns to count the signal pulses caused by the ions while impinging on the MCP. Furthermore, a fast timing amplifier (Ortec, model VT120 [88]) was used to amplify the current pulses generated by the MCP detector before sending them to the SR430. The accumulated counts are normalized to the number of cycles and thus an average count rate per ejection can be calculated. The prediction confidence interval for the average count rate is calculated from the standard deviation of all cycles which were used for averaging. While keeping the ejection time constant at 10 µs, the breeding time was increased incrementally from 2.5 ms to 100 ms. The data was acquired for several differently charged argon ions impinging on MCP1 behind the Wien filter (Fig. 4.7). The individual electrode potentials are listed in Tab. 4.5.

Table 4.5: Settings for the measurement of the argon charge-state distribution as a function of the breeding time (Fig. 4.7).

V_{DT1} (V)	1595	V_{extr} (V)	93	I_e (mA)	-4.7
V_{DT2} (V)	1600	V_f (V)	-1309	ejection time (µs)	10
V_{DT3} (V)	1550/1984	V_c (V)	-1373	I_{WF} (A)	2.3
V_{DT4} (V)	1850	V_a (V)	110	pressure (10^{-9} mbar)	2.2
V_{DT5} (V)	1750				

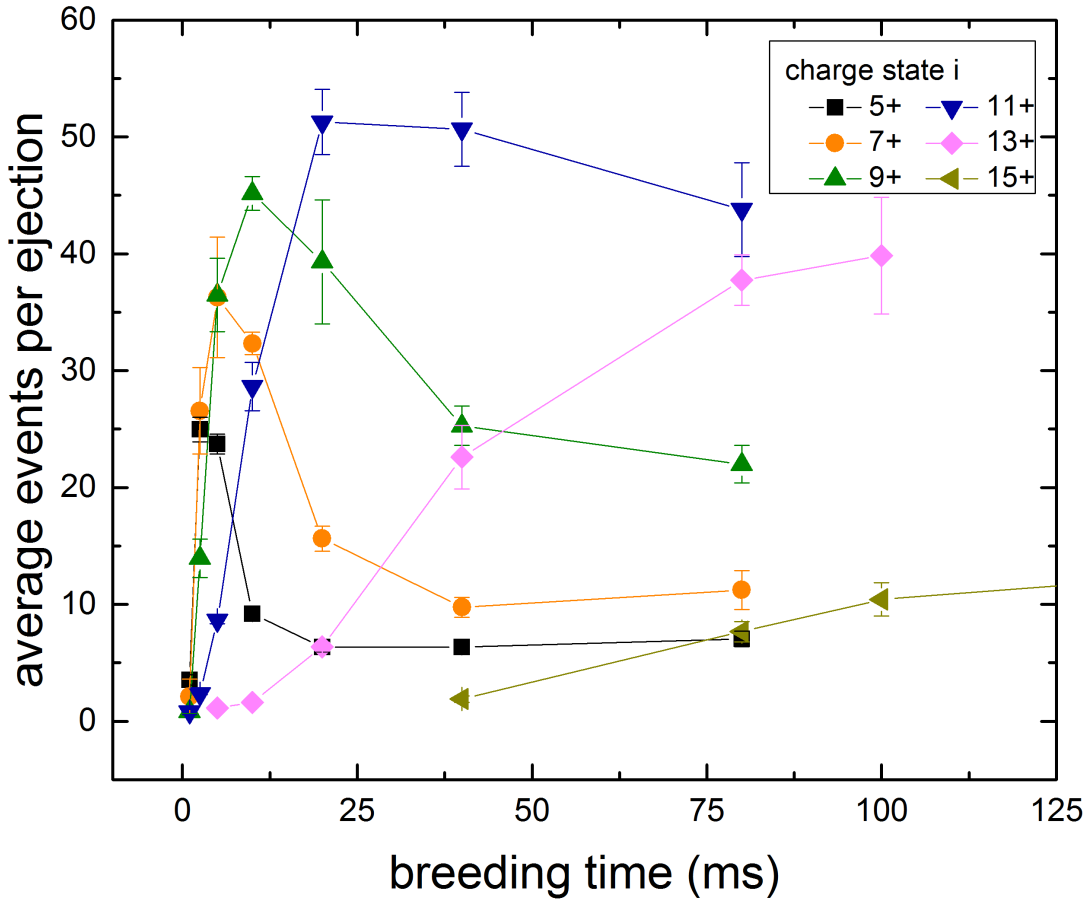

Figure 4.7: Abundance of different argon charge states as a function of the breeding time. Solid lines are a guide to the eye.

Similiar to the behavior predicted by the theoretical calculations (Fig. 3.3) and shown in section 3.2, each charge state reaches a maximum abundance at different breeding times.This observation can also seen in the charge-state distributions, where the center of the charge-state distribution is shifted depending on the breeding time. The higher the charge state, the later this maximum is reached.

Influence of the ejection time

In the pulsed mode of operation, the ions are trapped and the charge states are bred in the confining low potential configuration. The center region of this potential well can only take a certain amount of ions. Thus, the yield of ions depends on how efficiently the ions are ejected and will have a maximum determined by the initial number of ions which were trapped in the tt-EBIT. This was studied in this measurement series. For otherwise identical settings, the ejection time was varied from 0.1 µs to 1000 µs at a breeding time of 167 ms. The individual electrode potentials are listed in Tab. 4.6. The data were acquired for $^{40}Ar^{8+}$ ions impinging on MCP4.

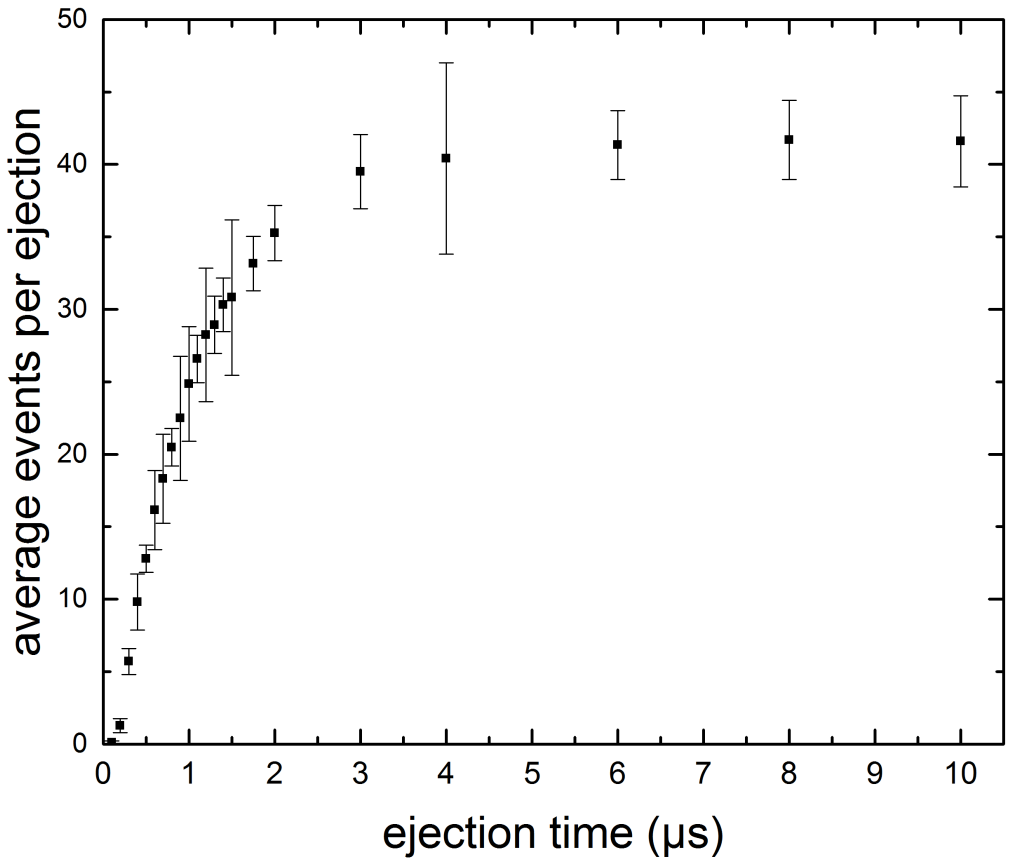

Figure 4.8: Number of $^{40}Ar^{8+}$ ions per ejection from the tt-EBIT as a function of the ejection time. The error is the standard deviation of the average counts per ejection.

Already an ejection time larger than 4 µs does not increase the count rate, which indicates a complete depletion of the ions from the trap region.

Table 4.6: Used settings for the measurement of the ejection time influence on the $^{40}Ar^{8+}$ ion yield (Fig. 4.8).

V_{DT1} (V)	1594	V_{extr} (V)	234	I_e (mA)	-4.7
V_{DT2} (V)	1600	V_f (V)	-1307	breeding time (ms)	167
V_{DT3} (V)	1500/2044	V_c (V)	-1372	I_{WF}(A)	1.5
V_{DT4} (V)	1814	V_a (V)	110	pressure (10^{-9} mbar)	3
V_{DT5} (V)	1659				

4.2 Demonstration of ion transport

In this section, the results of the transport of the ions through the beamline are presented. It was possible to obtain a focused ion beam at the last MCP detection unit behind the large ion optics (Fig. 4.9). After the large ion optics follows the last Einzel lens which is the last opportunity to manipulate the ion beam. For a successful injection into the Penning trap, the beam has to be precisely focused into the fringing field of superconducting solenoid magnet. The position of the focus has to be determined with high accuracy since at the entrance of the Penning trap a diaphragm of 3 mm (Fig. 3.8) is installed. This diaphragm serves as a limiting factor for radial ion motion when injected into the trap center and also as a pumping barrier. In addition it blocks heat radiation to reach the trap and is a dump for the millimeter waves. In the following, results of ToF measurements for decelerated ion bunches are presented.

Deceleration by the pulsed drift tube

For the injection and dynamic capture of the ions in the Penning trap their kinetic energy has to be below $\lesssim 200$ qV. The deceleration is done in the pulsed drift tube of the large ion optics. This section shows this procedure applied to $^{40}Ar^{9+}$ ion bunches extracted from the tt-EBIT. Fig. 4.10 shows the resulting ToF-distributions as a function of the lift electrode potential U_{lift}. The number of counts is again obtained by measuring the ion signal pulses of the MCP via the multichannel scaler. The pulsed drift tube electrode used in the large ion optic element has a length l_{lift} of 495 mm and an inner diameter of 50 mm. The flight time of ions that travel through the lift electrode is given by $t_{lift} = \frac{l_{lift}}{v_{ion}} = l_{lift}\sqrt{\frac{m_{ion}}{2q(U_{transfer}-U_{lift})}}$. A deceleration down to a kinetic energy of $q \times 200$ V leads to $t_{lift} \simeq 5.3$ µs for $^{40}Ar^{9+}$ and $t_{lift} \simeq 4.0$ µs for $^{208}Pb^{81+}$, respectively. In order to minimize the loss of ions during deceleration the whole ion bunch has to be in the pulsed section of the drift tube at the same time. This restricts the acceptable maximum width of the ToF of an incoming bunch. The time for switching of the voltage on an electrode with a fast high transistor switch (Behlke

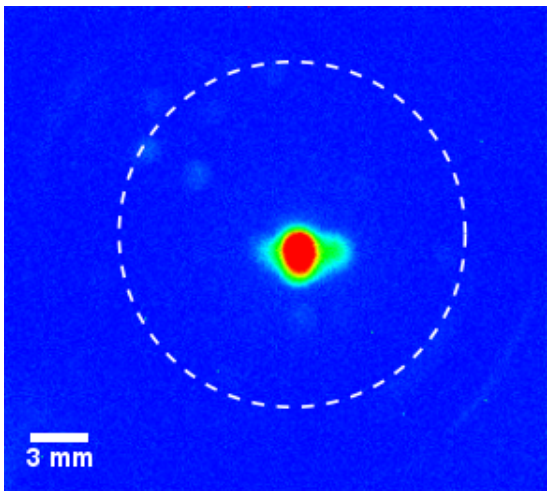

Figure 4.9: $^{40}Ar^{9+}$ ions on MCP4 at a deceleration voltage of 1950 V. This corresponds to a remaining kinetic energy of 9×65eV. The dotted circle denotes the active area of the MCP of a diameter of 18mm.

Power Electronics, model GHTS 100A [89]) is on the order of <100 ns for a load capacitance <500 pF. This kind of switch combines a large number of MOSFETs in series and paralell connections. By driving the individual MOSFETs synchronously and with a low impedance it is possible to obtain nanosecond transition times [89]. For each drift tube voltage, 9000 ejection cycles were accumulated.

Table 4.7: Used settings for the measurement of the ToF distributions of $^{40}Ar^{9+}$ ions as a function of the deceleration voltage (Fig. 4.10).

V_{DT1} (V)	1594	ejection time (µs)	1
V_{DT2} (V)	1600	breeding time (ms)	30
V_{DT3} (V)	1500/2044		
V_{DT4} (V)	1814		
V_{DT5} (V)	1659		

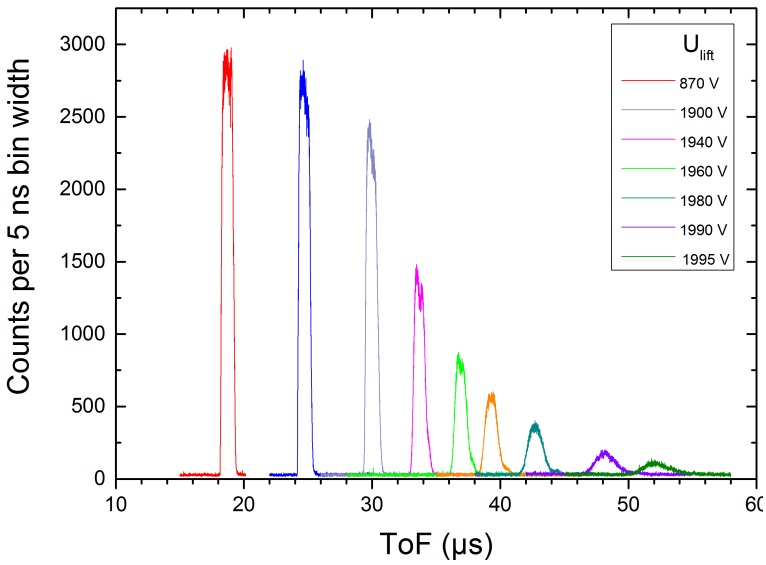

Figure 4.10: ToF distributions of $^{40}Ar^{9+}$ ions arriving on MCP4 for different lift electrode voltages U_{lift}. The bin width of the multichannel scaler was set to 5 ns. The ToF for the undecelarated ions with a transfer energy of 9×2015 eV is ≈ 18.7 µs and the counts are accumulated for 9000 ejections per voltage.

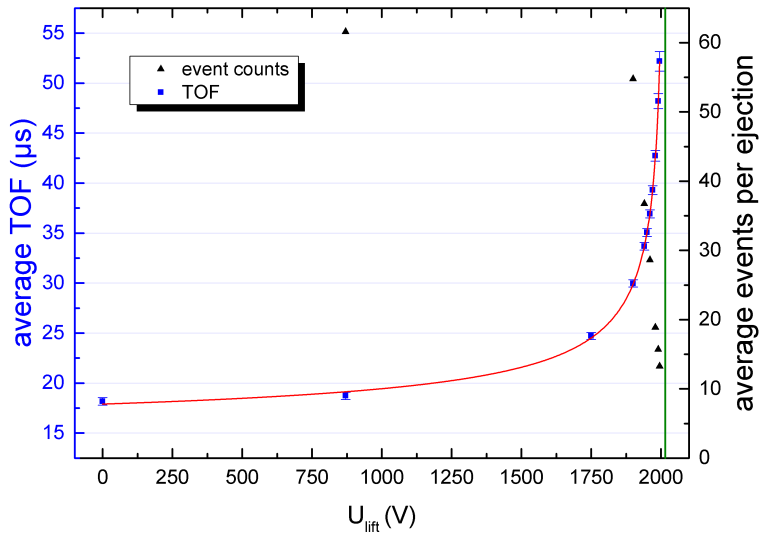

Figure 4.11: Average ToF as function of the deceleration potential U_{lift}. From the fit (for details see text) an initial starting potential of 2015(1) V can be estimated (green line).

From Fig. 4.10 can be seen that the width of the ToF distribution increases for higher deceleration potentials. At the same time the total number of ions is decreasing by a factor of 5 (Fig. 4.11). Using the average TOF data, the starting potential U_0 of the ions in the tt-EBIT can be estimated. Therefore, a simplified model is fitted to the ToF data. It is assumed that the ions propagate through the beamline with a constant average velocity. The total time of flight t_{total} can then be decomposed into a time t_1 in which the ions travel at the initial velocity a distance s_1 to the point of deceleration and into a time t_2, in which the ions propagate with their reduced velocity the distance s_2 until the MCP,

$$t_{\text{total}} = t_1 + t_2 = \frac{s_1}{\sqrt{cU_0}} + \frac{s_1}{\sqrt{c(U_0 - U_{\text{lift}})}}. \tag{4.1}$$

c equals $2q/m_{\text{ion}}$. The red line in Fig. 4.11 is a fit of equation (4.1) to the data. From this fit, the initial starting potential of $U_0 = 2015(1)\,\text{V}$ is derived, for which the ToF would diverge.

4.3 Conclusions

The main purpose of the tt-EBIT is to be used for the commissioning and tests of the beamline and the Penning-trap system. Two main criteria for a successful commissioning are:

The ion species extracted from the tt-EBIT has to meet the design parameter of the Penning-trap system such that the detection circuits and amplifiers can be tested. The yield and the transport efficiency of this ion species has to be high enough that an injection into the Penning trap is feasible in a reasonable time.

Test of the trap system

For the test of the detection of the ion's axial motion, its q/m ratio should be comparable to possible measurement candidates, in order to be able to detect a signal. Since the measurements are expected to be done for ions up to $^{208}\text{Pb}^{81+}$, in the following this ion species is used for a comparison with the properties of the extracted argon ions. The axial frequency can be calculated similar to the case of an ideal Penning trap (2.22) with an additional coefficient C_2 due to the trap geometry and can be calculated [40]. The axial frequency reads then

$$\nu_z = \frac{\omega_z}{2\pi} = \sqrt{\frac{q\Phi_0 C_2}{md^2}}, \tag{4.2}$$

where $C_2 = 0.59$ and $d = 9.16\,\text{mm}$ are the trap specific parameters for the precision trap of ALPHATRAP. The axial frequency for an ion can be changed via the trap potential which is restricted to $\Phi_0 < 100\,\text{V}$ for ALPHATRAP. For the detection

the resonance circuits have to be tuned to a predetermined value. Comparable to values in previous setups [5], the axial frequency axial frequency is here assumed to be 650 kHz, which results in a trap potential of $\Phi_0 \approx 63\,\mathrm{V}$ for $^{208}Pb^{81+}$ and $\Phi_0 \approx 98\,\mathrm{V}$ for $^{40}Ar^{10+}$, respectively. This axial frequency sets a limit to the minimum argon charge state, that can be trapped with a voltage $\Phi_0 < 100\,\mathrm{V}$. Therefore argon ions with a charge ≥ 10 have to be used.

Test of the ion injection

As seen in the previous section, for an assumed axial frequency of 650 kHz, argon ions in a charge state ≥ 10 are suitable candidates to be measured with this tuning of the axial circuit. In the following, the expected numbers of $^{40}Ar^{10+}$ ions per ejection cycle is roughly estimated.

Even though the data for the count rates at MCP4 behind the large ion optics were measured for $^{40}Ar^{8+}$, it can be seen from Fig. 4.5 that the count rate for $^{40}Ar^{10+}$ is approximately the same. Therefore, in the following considerations the count rate of $^{40}Ar^{8+}$ and $^{40}Ar^{10+}$ is to be assumed at least equal at MCP4. From Fig. 4.8 at least 40 events per ejection can be derived for the case of undecelerated ions. The efficiency of the MCP for positive ions can be estimated from literature [41, 90, 91] to be $\approx 50\%$, so that the actual number of ions is probably higher by a factor of ≈ 2. From Fig. 4.10 and Fig. 4.11 it can be estimated that the width of the ToF of the bunches is about 1 µs and shows less than 100 events per ejection, corresponding to a rate of $< 100\,\mathrm{MHz}$. The bandwidth of the preamplifier is 10 to 350 MHz and the maximum count rate of the MCA is 100 MHz. Even here a larger number of ions would be underestimated. So far the considerations about the detection efficiency lead to a countrate of $\approx 2 \times 40$ ions per ejection. Fig. 4.11 also shows that by the deceleration process from $q \times 1150\,\mathrm{V}$ to about $q \times 100\,\mathrm{V}$ remaining kinetic energy reduces the registered events per ejection by $\approx 10\%$. Thus still more about 70 ions per ejection could be focused on the opening diaphragm of the Penning trap, which blocks some of the ions. In order to get an estimate on this effect, the diameters of the diaphragm ($d_{\mathrm{dia}} = 3\,\mathrm{mm}$) and the spot size of the ion beam can be compared (Fig. 4.9). The diameter of the spot can be estimated as $d_{\mathrm{beam}} \simeq 4\,\mathrm{mm}$. Assuming a homogeneous distribution of the ions inside the beam, then the number of ions passing the diaphragm would decrease by a factor of $1 - \left(\frac{d_{dia}}{d_{beam}}\right)^2 \approx 0.44$. Therefore one would lose about 50% of the ions, and one could inject still about 35 ions per ejection from the tt-EBIT into the trap. Since the magnetic field gradient starts above the diaphragm, the magnetic field even supports the injection by guiding and compressing the beam assuming the beam were pointed to the correct radial position in the fringing field. Although final measurements remain to be done, this modest estimate based on simplified assumption should at least give an idea of the order of magnitude and that the number of extracted ions from the tt-EBIT is appropriate for the upcoming final commissioning.

4.4 Laser ablation source for beryllium ions

A future major step to reduce the measurement uncertainty and open up new physics possibilities at ALPHATRAP is the implementation of sympathetic laser cooling of HCIs. The laser cooling can be used the reduce the temperature of the HCIs even further than with the common techniques used in similar experiments so far, which results in a increased precision, see chapter 5. Because there are no optical transitions in the level structure of HCIs, they have to be cooled sympathetically by another ion species. In this method, different ions are cooled by their mutual Coulomb interactions. One ion species (for instance $^9Be^+$) is directly cooled by laser cooling, whereas the second ion species (a HCI) is cooled through the Coulomb interaction with the cooled ions species. Both can be cooled to a common equilibrium temperature. For this reason, a reliable and effective source for $^9Be^+$ ions is needed. In this section, the production of $^9Be^+$ in a laser ablation source is presented. For this purpose, a feasibility study was done in the context of this thesis at the TRIGA-TRAP experiment at the University of Mainz [92]. This double-Penning trap mass spectrometer experiment is equipped with a laser ablation source [93] and the group offered kind support for tests. In measurements for the TRIGA-TRAP experiment, carbon targets are used for the creation of singly charged carbon clusters as mass references. In the following measurement, a thin copper beryllium[2] foil was attached on the rotatable carbon target. Due to the toxicity of pure beryllium, in these first tests copper beryllium was used since this alloy in solid form has no known health hazard. The main goal was to see if it is feasible to use a laser ablation source for the production of singly charged $^9Be^+$ ions despite its high first ionization potential of 9.32 eV [84]. A pulse from a frequency doubled Nd:YAG laser[3] is focused on the target. Some of the material is explosively ablated and transformed into a dense plasma plume in which electron-ion thermalization takes place and a distribution of typically low charge states is created [94]. The ions are extracted and by a radiofrequency quadrupole structure guided into the beamline of the TRIGA-TRAP experiment, where a ToF distribution can be measured (Fig. 4.12). The calibration for the ToF spectrum is done by using charge-to-mass ratios of well known reference ions. The time of flight t_i of one ion with charge q_{ion} and mass m_{ion} is $\propto \sqrt{m_{\text{ion}}/q_{\text{ion}}}$ and therefore for different ion species one obtains[4]:

$$t_i = t_{\text{ref}} \sqrt{\frac{q_{\text{ref}}}{q_i} \frac{m_i}{m_{\text{ref}}}}. \tag{4.3}$$

For the calibration, the laser is focused on a carbon target. As reference ion, the highly abundant alkali ion $^{39}K^+$ is used and the obtained calibration shows good agreement with other ambient ion species such as singly charged $^{14}N_2^+$, $^{16}O_2^+$, $^{16}N^+$

[2] CuBe, compositon by mass: 98% Cu, 2%Be, Ni+Co 500-4000 ppm

[3] $\lambda = 532$ nm, typical parameters: pulse length 5 ns, focus diameter $\simeq 0.85$ mm, power density 120 - 250 MW/cm^2, repetition rate $\leq$1 Hz

[4] The time offset in the TOF due to signal transit time, which is in the order of 0.1 µs to 0.5 µs, is neglected here.

and carbon clusters C_7^+ to C_{11}^+ (Fig. 4.13). Immediately after the calibration, the target was rotated and the laser pulse now hit the CuBe foil. A ToF spectrum (Fig. 4.14) was acquired by accumulating the spectra for 759 laser shots and $^9Be^+$ were unambigiously created. The number of total counts for the range 9 u to 16 u is 190 and 1720 for the range from 29 u to 74 u. This corresponds to ≈ 0.25 Be and ≈ 2.25 Cu ions detected per laser shot[5]. From the analysis of the individual spectra per laser shot can be seen, that the abundance of Cu ions is typically in the range of 10 to 30 ions per laser shot and the width of the ToF is about 1.8 µs. This can lead to a saturation of the detection [95] and hence the number of Cu ions can be underestimated. However this does not affect the count rate of the Be ions. This is certainly not the maximum achievable yield of Be ions. The measurements and especially the extraction were not optimized for a maximum yield of light ions, since it is usually used for heavier carbon clusters. The yield could be increased by using a pure Be foil instead of CuBe and it was observed that the total yield also depended on the laser pulse power.

The envisaged sympathetic laser cooling for the ALPHATRAP experiment relied on the reliable production of $^9Be^+$ ions. These results confirmed that a laser ablation source can be used for the production of singly charged beryllium ions and these ions could then be injected into the Penning-trap system for sympathetic laser cooling at ALPHATRAP. Therefore this measurement triggered the development of the FEP ion source as an intermediate in-trap source for beryllium (section 3.8) and furthermore initiated the development of an own laser ablation source for the ALPHATRAP experiment for the long term.

[5] This number is the detected events. Due to extraction, transport and detection efficiencies, the actual number of created beryllium ions is supposedly higher.

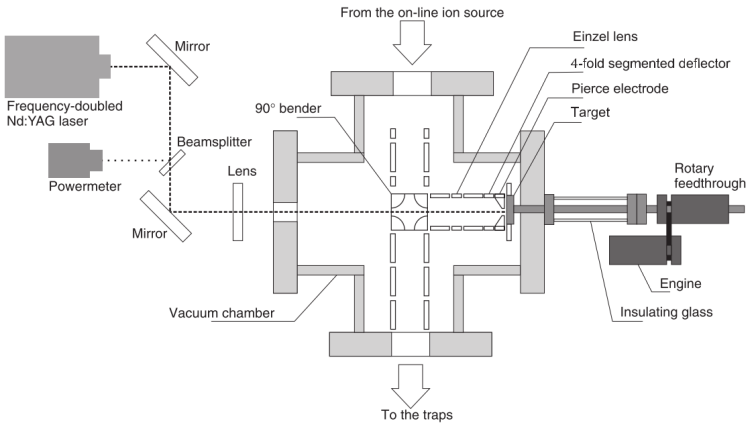

Figure 4.12: Sketch of the laser ablation ion source at TRIGA-TRAP. The produced ions are extracted with an extraction with an extraction plate of Pierce geometry and the radiofrequency quadrupole structure and by the 90° electrostatic bender deflected into the beamline for the ToF measurement [93].

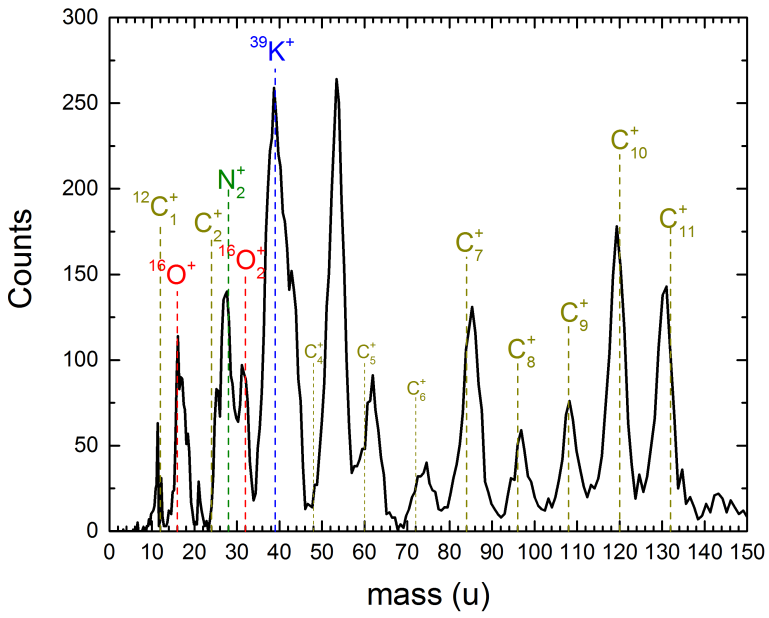

Figure 4.13: Laser ablation spectrum for a carbon target. For the calibration of the ToF, $^{39}K^{+}$ was used.

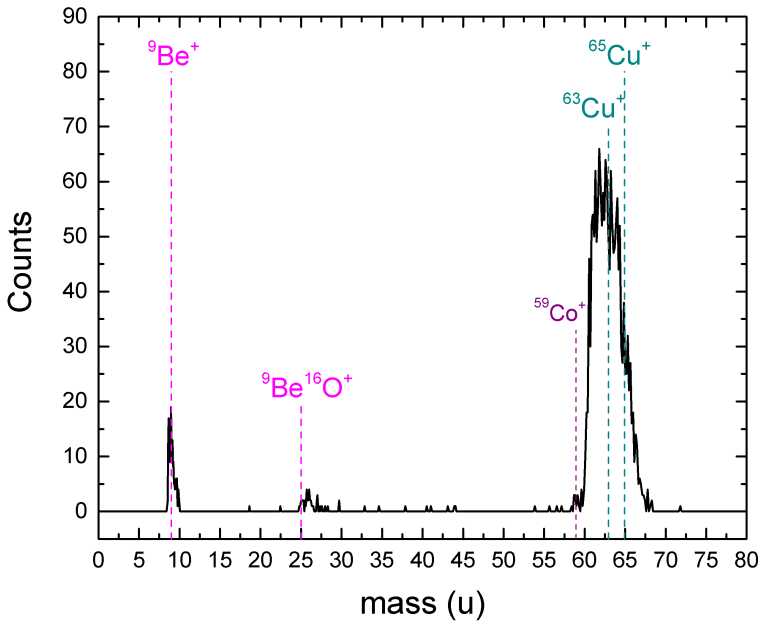

Figure 4.14: Laser ablation spectrum for a CuBe target. For details see text.

5 Outlook

The aim of this work was the setup and commissioning of the ALPHATRAP beamline. For this purpose, a characterization of a compact room-temperature tt-EBIT was carried out, which serves as an ion source for testing the beamline. In the future, this tt-EBIT will be used to provide highly charged ions for the commissioning of the final beamline setup and the Penning-trap system including the injection and storage of these ions.

It was shown that with the current setup ions with an ionization potential up to 0.9 keV can be produced, such as boron-like and lithium-like argon ions. These were extracted in bunches and subsequently transported through the beamline. For a successful injection of highly charged ions into the Penning-trap system, the ion bunches have to be decelerated by a pulsed drift tube. The operation of important ion-optical elements and the pulsed drift tube could be confirmed. The measurements presented here were performed with the beamline setup in an separate offline laboratory. The operating parameters found in this testing phase will serve as starting point for the upcoming beamline commissioning at its final position. The relocation of the ALPHATRAP beamline from its offline location to the final setup next to the Heidelberg EBIT was prepared and completed. During this process, the beamline was disassembled into its individual elements and rebuilt at its final position in the experimental hall. There, it was mounted on a new support structure and aligned with respect to the other components such as the magnet. The cryostat mounted on top of the magnet was also assembled and inserted into the magnet. The magnet became operational as well and was charged to a magnetic field of 4.02 T.

Moreover, the preparation for an extension of the ALPHATRAP experiment was carried out. In a next phae, the ALPHATRAP experiment will be equipped with the possibility of sympathetic laser cooling, improving the experimental system considerably:

First of all, a reduction of the temperature is equivalent to a reduction of the amplitudes[1] of the ion's motional eigenmodes. By this the ions are confined in a smaller space, which makes them less sensitive to anharmonicities in the trapping fields and energy dependent frequency shifts and will increase the achievable precision. The precision for the measurement of the modified cyclotron frequency ν_+ by the phase-sensitive technique, the pulse and amplify (PnA) method, will be improved by lower temperatures. Since ν_+ represents the largest contribution to the free cyclotron frequency a more precise measurement with a lower thermal phase jitter will increase

[1] In a Penning trap reducing the amplitudes of motion means decreasing the energy in the cyclotron and axial mode, whereas energy has to be added to the magnetron mode.

the precision in the determination of the free cyclotron frequency.The detection of the spin flip in the AT via the axial frequency shift $\Delta\omega_z \propto \frac{1}{\sqrt{m_{ion}}}$ is a challenge when going to heavier ions. Since the dipole heating rate in the cylcotron mode scales with the energy in this mode, further cooling would decrease this rate and facilitate the detection of the spin flip [96].

As prearrangement for this upgrade, the possibilities for $^{9}Be^{+}$ ion sources were explored. Measurements with a laser ablation source at the TRIGA-TRAP experiment in Mainz confirmed the capability of this type of ion source to produce these ions in sufficient amount. This led to the start of the development of a custom made laser ablation source for the ALPHATRAP experiment. In the medium term, in order to have an ion source for tests and commissioning of the Penning-trap system available, a field emission point ion source was designed and went into production. This field emission ion source is mounted below the Penning-trap system and allows an in-trap production of ions. With these sources, and the ongoing final assembly of the remaining experimental setup, ALPHATRAP will soon start to test bound-state quantum electrodynamics under extreme conditions.

6 Bibliography

[1] R. S. Van Dyck, P. B. Schwinberg, H. G. Dehmelt, New high-precision comparison of electron and positron g factors, Physical Review Letters 59 (1987) 26–29. doi:10.1103/PhysRevLett.59.26.

[2] D. Hanneke, S. Fogwell, G. Gabrielse, New measurement of the electron magnetic moment and the fine structure constant, Physical Review Letters 100 (2008) 120801. doi:10.1103/PhysRevLett.100.120801.

[3] H. Häffner, T. Beier, N. Hermanspahn, H.-J. Kluge, W. Quint, S. Stahl, J. Verdú, G. Werth, High-accuracy measurement of the magnetic moment anomaly of the electron bound in hydrogenlike carbon, Physical Review Letters 85 (25) (2000) 5308. doi:10.1103/PhysRevLett.85.5308.

[4] J. Verdú, S. Djekić, S. Stahl, T. Valenzuela, M. Vogel, G. Werth, T. Beier, H.-J. Kluge, W. Quint, Electronic g factor of hydrogenlike oxygen $^{16}O^{7+}$, Physical Review Letters 92 (9) (2004) 093002. doi:10.1103/PhysRevLett.92.093002.

[5] S. Sturm, A. Wagner, B. Schabinger, J. Zatorski, Z. Harman, W. Quint, G. Werth, C. H. Keitel, K. Blaum, g factor of hydrogenlike $^{28}Si^{13+}$, Physical Review Letters 107 (2011) 023002. doi:10.1103/PhysRevLett.107.023002.

[6] T. Aoyama, M. Hayakawa, T. Kinoshita, M. Nio, Tenth-order qed contribution to the electron $g-2$ and an improved value of the fine structure constant, Physical Review Letters 109 (2012) 111807. doi:10.1103/PhysRevLett.109.111807.

[7] K. Pachucki, A. Czarnecki, U. D. Jentschura, V. A. Yerokhin, Complete two-loop correction to the bound-electron g factor, Physical Review A 72 (2005) 022108. doi:10.1103/PhysRevA.72.022108.

[8] V. M. Shabaev, V. A. Yerokhin, Recoil correction to the bound-electron g factor in h-like atoms to all orders in αZ, Physical Review Letters 88 (2002) 091801. doi:10.1103/PhysRevLett.88.091801.

[9] Experimental Setup in Mainz, The g-factor of highly charged ions - Blaum Division, Max-Planck-Institut für Kernphysik, Heidelberg.
URL https://www.mpi-hd.mpg.de/blaum/gfactor/silicon/index.en.html#setup

[10] The nobel prize in physics 1965 (1965).
URL http://www.nobelprize.org/nobel_prizes/physics/laureates/1965/index.html

[11] W. E. Lamb Jr, R. C. Retherford, Fine structure of the hydrogen atom by a microwave method, Physical Review 72 (3) (1947) 241. doi:10.1103/PhysRev.72.241.

[12] M. Lochmann, R. Jöhren, C. Geppert, Z. Andelkovic, D. Anielski, B. Botermann, M. Bussmann, A. Dax, N. Frömmgen, M. Hammen, V. Hannen, T. Kühl, Y. A. Litvinov, R. López-Coto, T. Stöhlker, R. C. Thompson, J. Vollbrecht, A. Volotka, C. Weinheimer, W. Wen, E. Will, D. Winters, R. Sánchez, W. Nörtershäuser, Observation of the hyperfine transition in lithium-like bismuth $^{209}Bi^{80+}$: Towards a test of QED in strong magnetic fields, Physical Review A 90 (2014) 030501. doi:10.1103/PhysRevA.90.030501.

[13] R. Bouchendira, P. Cladé, S. Guellati-Khélifa, F. Nez, F. Biraben, New determination of the fine structure constant and test of the quantum electrodynamics, Physical Review Letters 106 (2011) 080801. doi:10.1103/PhysRevLett.106.080801.

[14] W. Quint, M. Vogel, Fundamental Physics in Particle Traps, Springer Tracts in Modern Physics, Springer Berlin Heidelberg, 2014. doi:10.1007/978-3-642-45201-7.

[15] P. A. M. Dirac, The quantum theory of the electron, in: Proceedings of the Royal Society of London A: Mathematical, Physical and Engineering Sciences, Vol. 117, The Royal Society, 1928, pp. 610–624. doi:10.1098/rspa.1928.0023.

[16] P. Kusch, H. M. Foley, Precision measurement of the ratio of the atomic 'g values' in the $^2p_{\frac{3}{2}}$ and $^2p_{\frac{1}{2}}$ states of gallium, Physical Review 72 (1947) 1256–1257. doi:10.1103/PhysRev.72.1256.2.

[17] J. Schwinger, On quantum-electrodynamics and the magnetic moment of the electron, Physical Review 73 (1948) 416–417. doi:10.1103/PhysRev.73.416.

[18] T. Aoyama, M. Hayakawa, T. Kinoshita, M. Nio, Tenth-order electron anomalous magnetic moment: Contribution of diagrams without closed lepton loops, Physical Review D 91 (2015) 033006. doi:10.1103/PhysRevD.91.033006.

[19] G. Breit, The magnetic moment of the electron., Nature 122 (1928) 649. doi:10.1038/122649a0.

[20] F. Köhler, S. Sturm, A. Kracke, G. Werth, W. Quint, K. Blaum, The electron mass from g-factor measurements on hydrogen-like carbon $^{12}C^{5+}$, Journal of

Physics B: Atomic, Molecular and Optical Physics 48 (14) (2015) 144032. doi:10.1088/0953-4075/48/14/144032.

[21] K. Blaum, High-accuracy mass spectrometry with stored ions, Physics Reports 425 (1) (2006) 1 – 78. doi:10.1016/j.physrep.2005.10.011.

[22] F. Köhler, K. Blaum, M. Block, S. Chenmarev, S. Eliseev, D. A. Glazov, M. Goncharov, J. Hou, A. Kracke, D. A. Nesterenko, et al., Isotope dependence of the *z*eeman effect in lithium-like calcium, Nature communications 7 (2016) 10246. doi:10.1038/ncomms10246.

[23] J. Zatorski, N. S. Oreshkina, C. H. Keitel, Z. Harman, Nuclear shape effect on the *g* factor of hydrogenlike ions, Physical Review Letters 108 (2012) 063005. doi:10.1103/PhysRevLett.108.063005.

[24] G. Werth, J. Alonso, T. Beier, K. Blaum, S. Djekic, H. Häffner, N. Hermanspahn, W. Quint, S. Stahl, J. Verdú, T. Valenzuela, M. Vogel, Highly charged ions, quantum-electrodynamics, and the electron mass, International Journal of Mass Spectrometry 251 (2–3) (2006) 152 – 158. doi:10.1016/j.ijms.2006.01.046.

[25] A. Wagner, S. Sturm, F. Köhler, D. A. Glazov, A. V. Volotka, G. Plunien, W. Quint, G. Werth, V. M. Shabaev, K. Blaum, *g* factor of lithiumlike silicon $^{28}Si^{11+}$, Physical Review Letters 110 (2013) 033003. doi:10.1103/PhysRevLett.110.033003.

[26] G. V. Dunne, New strong-field QED effects at ELI: nonperturbative vacuum pair production (2008). arXiv:0812.3163.

[27] W. Heisenberg, H. Euler, Folgerungen aus der Diracschen Theorie des Positrons, Zeitschrift für Physik 98 (11) (1936) 714–732. doi:10.1007/BF01343663.

[28] F. Sauter, Über das Verhalten eines Elektrons im homogenen elektrischen Feld nach der relativistischen Theorie Diracs, Zeitschrift für Physik 69 (11-12) (1931) 742–764. doi:10.1007/BF01339461.

[29] T. Beier, I. Lindgren, H. Persson, S. Salomonson, P. Sunnergren, H. Häffner, N. Hermanspahn, g_j factor of an electron bound in a hydrogenlike ion, Physical Review A 62 (3) (2000) 032510. doi:10.1103/PhysRevA.62.032510.

[30] J. Scofield, Ionization Energies, LLNL Internal Report, Livermore, CA 94550, USA (2001).

[31] J. R. C. López-Urrutia, J. Braun, G. Brenner, H. Bruhns, A. Lapierre, A. J. G. Martínez, V. Mironov, R. S. Orts, H. Tawara, M. Trinczek, et al., Optimization of the charge state distribution of the ion beam extracted from an EBIT by

dielectronic recombination, Review of Scientific Instruments 75 (5) (2004) 1560–1562. doi:10.1063/1.1691521.

[32] L. Buchauer, Konstruktion einer kompakten Elektronenstrahl-Ionenfalle mit Permanentmagneten für Fluoreszenzmessungen, Bachelor's Thesis, Max-Planck-Institut für Kernphysik (2012).

[33] S. Sturm, F. Köhler, J. Zatorski, A. Wagner, Z. Harman, G. Werth, W. Quint, C. H. Keitel, K. Blaum, High-precision measurement of the atomic mass of the electron, Nature 506 (7489) (2014) 467–470. doi:10.1038/nature13026.

[34] P. J. Mohr, D. B. Newell, B. N. Taylor, CODATA Recommended Values of the Fundamental Physical Constants: 2014 (2015). arXiv:1507.07956.

[35] V. M. Shabaev, D. A. Glazov, N. S. Oreshkina, A. V. Volotka, G. Plunien, H.-J. Kluge, W. Quint, *g*-factor of heavy ions: A new access to the fine structure constant, Physical Review Letters 96 (2006) 253002. doi:10.1103/PhysRevLett.96.253002.

[36] The Nobel Prize in Physics 1989 (1989).
URL http://www.nobelprize.org/nobel_prizes/physics/laureates/1989/

[37] J. D. Jackson, Classical Electrodynamics, Wiley, New York, 1999.

[38] F. G. Major, V. N. Gheorghe, G. Werth, Charged Particle Traps, Vol. 37 of Springer Series on Atomic, Optical, and Plasma Physics, Springer-Verlag Berlin Heidelberg, 2005. doi:10.1007/b137836.

[39] The Nobel Prize in Physics 1989, Hans G. Dehmelt Biographical (1989).
URL http://www.nobelprize.org/nobel_prizes/physics/laureates/1989/dehmelt-bio.html

[40] G. Gabrielse, L. Haarsma, S. Rolston, Open-endcap Penning traps for high precision experiments, International Journal of Mass Spectrometry and Ion Processes 88 (2) (1989) 319 – 332. doi:10.1016/0168-1176(89)85027-X.

[41] Lecture notes "Stored Charged Particles" by Prof. K. Blaum and Dr. Sven Sturm, Heidelberg University, winter term 2015/16.
URL https://www.mpi-hd.mpg.de/blaum/teaching/2015/ws1516_stored-particles/content.en.html

[42] L. S. Brown, G. Gabrielse, Geonium theory: Physics of a single electron or ion in a Penning trap, Review of Modern Physics 58 (1986) 233–311. doi:10.1103/RevModPhys.58.233.

[43] K. Blaum, Sz. Nagy, G. Werth, High-accuracy Penning trap mass measurements with stored and cooled exotic ions, Journal of Physics B: Atomic, Molecular and Optical Physics 42 (15) (2009) 154015. doi:10.1088/0953-4075/42/15/154015.

[44] S. Sturm, The g-factor of the electron bound in $^{28}Si^{13+}$: The most stringent test of bound-state quantum electrodynamics, Ph.D. thesis, Johannes-Gutenberg Universität, Mainz (2012).
URL http://ubm.opus.hbz-nrw.de/volltexte/2012/3108/

[45] A. Weigel, Entwicklung des kryogenen Nachweissystems für ALPHATRAP und THe-Trap, Master's Thesis, Max-Planck-Institut für Kernphysik (2014).
URL http://hdl.handle.net/11858/00-001M-0000-0024-469B-E

[46] H. Dehmelt, Continuous Stern-Gerlach effect: Principle and idealized apparatus, Proceedings of the National Academy of Sciences 83 (8) (1986) 2291–2294.
URL http://www.ncbi.nlm.nih.gov/pmc/articles/PMC323282/

[47] R. S. van Dyck, P. Ekstrom, H. Dehmelt, Axial, magnetron, cyclotron and spin-cyclotron-beat frequencies measured on single electron almost at rest in free space (geonium), Nature 262 (1976) 776–777. doi:10.1038/262776a0.

[48] H. Häffner, T. Beier, S. Djekić, N. Hermanspahn, H.-J. Kluge, W. Quint, S. Stahl, J. Verdú, T. Valenzuela, G. Werth, Double Penning trap technique for precise g factor determinations in highly charged ions, The European Physical Journal D - Atomic, Molecular, Optical and Plasma Physics 22 (2) (2003) 163–182. doi:10.1140/epjd/e2003-00012-2.

[49] T. Beier, H. Häffner, N. Hermanspahn, S. G. Karshenboim, H.-J. Kluge, W. Quint, S. Stahl, J. Verdú, G. Werth, New determination of the electron's mass, Physical Review Letters 88 (2001) 011603. doi:10.1103/PhysRevLett.88.011603.

[50] H. Häffner, T. Beier, N. Hermanspahn, H.-J. Kluge, W. Quint, S. Stahl, J. Verdú, G. Werth, High-accuracy measurement of the magnetic moment anomaly of the electron bound in hydrogenlike carbon, Physical Review Letters 85 (2000) 5308–5311. doi:10.1103/PhysRevLett.85.5308.

[51] J. R. C. López-Urrutia, J. Braun, G. Brenner, H. Bruhns, C. Dimopoulou, I. N. Draganić, D. Fischer, A. J. G. Martínez, A. Lapierre, V. Mironov, R. Moshammer, R. S. Orts, H. Tawara, M. Trinczek, J. Ullrich, Progress at the Heidelberg EBIT, Journal of Physics: Conference Series 2 (1) (2004) 42. doi:10.1088/1742-6596/2/1/006.

[52] A. J. G. Martínez, J. R. C. López-Urrutia, D. Fischer, R. S. Orts, J. Ullrich, The Heidelberg EBIT: Present results and future perspectives, Journal of Physics:

Conference Series 72 (1) (2007) 012001. doi:10.1088/1742-6596/72/1/012001.

[53] Agilent Technologies - ConFlat Flanges & Fittings, Agilent Technologies, Inc., 5301 Stevens Creek Blvd, Santa Clara, CA 95051, USA.
URL https://www.agilent.com/en-us/products/vacuum-technologies/vacuum-components/vacuum-flanges-fittings/conflat-flanges-fittings

[54] M. T. Orešković, Development of a cryogenic vacuum valve and an electromechanical switch for ALPHATRAP, Master's Thesis, Max-Planck-Institut für Kernphysik (2014).
URL http://hdl.handle.net/11858/00-001M-0000-0015-8372-F

[55] Edwards Vacuum, Edwards, Manor Royal, Crawley, West Sussex, RH10 9LW, United Kingdom.
URL https://www.edwardsvacuum.com/

[56] SAES - group, SAES Getters, S.p.A., Viale Italia 77, 20020 Lainate (Milan), Italy.
URL https://www.saesgetters.com

[57] Agilent Technologies - Ion Pumps, Agilent Technologies, Inc., 5301 Stevens Creek Blvd, Santa Clara, CA 95051, USA.
URL http://www.agilent.com

[58] R. Calder, G. Lewin, Reduction of stainless-steel outgassing in ultra-high vacuum, British Journal of Applied Physics 18 (10) (1967) 1459. doi:10.1088/0508-3443/18/10/313.

[59] V. P. Ovsyannikov, G. Zschornack, First investigations of a warm electron beam ion trap for the production of highly charged ions, Review of Scientific Instruments 70 (6) (1999) 2646–2651. doi:10.1063/1.1149822.

[60] CAD model courtesy of P. Micke, private communication.

[61] B. M. Penetrante, J. N. Bardsley, D. DeWitt, M. Clark, D. Schneider, Evolution of ion-charge-state distributions in an electron-beam ion trap, Physical Review A 43 (1991) 4861–4872. doi:10.1103/PhysRevA.43.4861.

[62] W. Lotz, An empirical formula for the electron-impact ionization cross-section, Zeitschrift für Physik 206 (2) (1967) 205–211. doi:10.1007/BF01325928.

[63] D. Schneider, M. W. Clark, B. M. Penetrante, J. McDonald, D. DeWitt, J. N. Bardsley, Production of high-charge-state thorium and uranium ions in an electron-beam ion trap, Physical Review A 44 (1991) 3119–3124. doi:10.1103/PhysRevA.44.3119.

[64] J. Orloff, Handbook of Charged Particle Optics, Second Edition, CRC Press, 2008.

[65] G. Herrmann, Optical theory of thermal velocity effects in cylindrical electron beams, Journal of Applied Physics 29 (2) (1958) 127–136. doi:10.1063/1.1723053.

[66] K. Amboss, Studies of a magnetically compressed electron beam, IEEE Transactions on Electron Devices 16 (11) (1969) 897–904. doi:10.1109/T-ED.1969.16878.

[67] A. Silze, G. Zschornack, V. P. Ovsyannikov, F. Ullmann, Properties of the electron beam in a room-temperature electron beam ion source investigated by position sensitive X-ray detection, Review of Scientific Instruments 79 (8). doi:10.1063/1.2960568.

[68] F. Dunning, R. Hulet, Atomic, Molecular, and Optical Physics: Charged Particles, Experimental Methods in the Physical Sciences, Elsevier Science, 1995.

[69] T. M. Bücking, An Off-Axis Electron Gun for a Compact Electron Beam Ion Trap, Master's Thesis, Max-Planck-Institut für Kernphysik (2013).
URL http://hdl.handle.net/11858/00-001M-0000-0013-F885-7

[70] P. Kruit, F. H. Read, Magnetic field paralleliser for 2π electron-spectrometer and electron-image magnifier, Journal of Physics E: Scientific Instruments 16 (4) (1983) 313. doi:10.1088/0022-3735/16/4/016.

[71] Colutron Research Cooperation, now offered and supported by Beam Imaging Solutions, Inc.
URL http://www.colutron.com

[72] S. Krämer, Aufbau und Charakterisierung eines Geschwindigkeitsfilters für das ALPHATRAP-Experiment, Bachelor's Thesis, Max-Planck-Institut für Kernphysik (2014).
URL http://hdl.handle.net/11858/00-001M-0000-0024-48CC-E

[73] J. L. Wiza, Microchannel plate detectors, Nuclear Instruments and Methods 162 (1) (1979) 587–601. doi:10.1016/0029-554X(79)90734-1.

[74] Advanced Performance Detectors - Selection Guide, Photonis USA, Inc., 660 Main Street, Sturbridge, MA 01566 - 1159, USA.
URL https://www.photonis.com/uploads/literature/apd/APD-Selection-Guide.pdf

[75] Prosilica GC 655, Allied Vision Technlogies, Taschenweg 2A, 07646 Stadtroda, Germany.

URL https://www.alliedvision.com/de/produkte/kameras/kameradetails/Prosilica%20GC/655.html

[76] HAMAMATSU MCP & MCP assembly guide, HAMAMATSU PHOTONICS K.K., Electron Tube Division, 314-5, Shimokanzo, Iwata City, Shizuoka Pref., 438-0193, Japan.
URL www.hamamatsu.com

[77] R. N. Wolf, G. Marx, M. Rosenbusch, L. Schweikhard, Static-mirror ion capture and time focusing for electrostatic ion-beam traps and multi-reflection time-of-flight mass analyzers by use of an in-trap potential lift, International Journal of Mass Spectrometry 313 (2012) 8 – 14. doi:10.1016/j.ijms.2011.12.006.

[78] G. Rouleau, H. Borgenstrand, C. Carlberg, S. R., F. Söderberg, I. Bergström, R. Jertz, T. Schwarz, J. Stein, G. Bollen, H. J. Kluge, R. Mann, The SMILETRAP (Stockholm-Mainz-Ion-Levitation-trap) facility, Hyperfine Interactions 99 (1) (1999) 73–81. doi:10.1007/BF02274910.

[79] Oxford Instruments, Oxford Instruments, plc, Tubney Woods, Abingdon, Oxfordshire, OX13 5QX, United Kingdom.
URL http://www.oxford-instruments.com/

[80] DuPont - Vespel parts and shapes, E. I. du Pont de Nemours and Company, 1007 Market Street, Wilmington, DE 19898, USA.
URL http://www.dupont.com/products-and-services/plastics-polymers-resins/parts-shapes/brands/vespel-polyimide.html

[81] C. Smorra, K. Blaum, L. Bojtar, M. Borchert, K. Franke, T. Higuchi, N. Leefer, H. Nagahama, Y. Matsuda, A. Mooser, M. Niemann, C. Ospelkaus, W. Quint, G. Schneider, S. Sellner, T. Tanaka, S. Van Gorp, J. Walz, Y. Yamazaki, S. Ulmer, BASE – The Baryon Antibaryon Symmetry Experiment, The European Physical Journal Special Topics 224 (16) (2015) 3055–3108. doi:10.1140/epjst/e2015-02607-4.

[82] Vacuumschmelze - Vacodur, Vacuumschmelze GmbH & Co. KG, Grüner Weg 37, 63450 Hanau, Germany.
URL http://www.vacuumschmelze.de/

[83] R. H. Fowler, L. Nordheim, Electron emission in intense electric fields, Proceedings of the Royal Society of London A: Mathematical, Physical and Engineering Sciences 119 (781) (1928) 173–181. doi:10.1098/rspa.1928.0091.

[84] A. Kramida, W. C. Martin, A compilation of energy levels and wavelengths for the spectrum of neutral beryllium (Be I), Journal of Physical and Chemical Reference Data 26 (5) (1997) 1185–1194. doi:10.1063/1.555999.

[85] H. Hirzler, Aufbau und Test der Transferbeamline für das ALPHATRAP Projekt, Bachelor's Thesis, Max-Planck-Institut für Kernphysik (2014).
URL http://hdl.handle.net/11858/00-001M-0000-0024-4693-D

[86] P. Mandal, G. Sikler, M. Mukherjee, Simulation study and analysis of a compact einzel lens-deflector for low energy ion beam, Journal of Instrumentation 6 (02) (2011) P02004. doi:10.1088/1748-0221/6/02/P02004.

[87] Stanford Research Systems - SR 430, Stanford Research Systems Inc., 1290-D Reamwood Avenue, Sunnyvale, CA 94089, USA.
URL http://www.thinksrs.com/

[88] Ortec Electronic Instruments, Ortec, 801 South Illinois Ave, Oak Ridge, TN 37830, USA.
URL http://www.ortec-online.com/

[89] Behlke - Fast High Voltage Power Switches, Behlke Power Electronics GmbH, Am Auernberg 4, 61476 Kronberg am Taunus, Germany.
URL http://www.behlke.com/pdf/general.pdf

[90] B. Brehm, J. Grosser, T. Ruscheinski, M. Zimmer, Absolute detection efficiencies of a microchannel plate detector for ions, Measurement Science and Technology 6 (7) (1995) 953. doi:10.1088/0957-0233/6/7/015.

[91] J. Oberheide, P. Wilhelms, M. Zimmer, New results on the absolute ion detection efficiencies of a microchannel plate, Measurement Science and Technology 8 (4) (1997) 351. doi:10.1088/0957-0233/8/4/001.

[92] J. Ketelaer, J. Krämer, D. Beck, K. Blaum, M. Block, K. Eberhardt, G. Eitel, R. Ferrer, C. Geppert, S. George, F. Herfurth, J. Ketter, Sz. Nagy, D. Neidherr, R. Neugart, W. Nörtershäuser, J. Repp, C. Smorra, N. Trautmann, C. Weber, Triga-spec: A setup for mass spectrometry and laser spectroscopy at the research reactor TRIGA mainz, Nuclear Instruments and Methods in Physics Research Section A: Accelerators, Spectrometers, Detectors and Associated Equipment 594 (2) (2008) 162 – 177. doi:10.1016/j.nima.2008.06.023.

[93] C. Smorra, K. Blaum, K. Eberhardt, M. Eibach, J. Ketelaer, J. Ketter, K. Knuth, Sz. Nagy, A carbon-cluster laser ion source for TRIGA-TRAP, Journal of Physics B: Atomic, Molecular and Optical Physics 42 (15) (2009) 154028. doi:10.1088/0953-4075/42/15/154028.

[94] M. Trinczek, A. Werdich, V. Mironov, P. Guo, A. G. Martínez, J. Braun, J. C. López-Urrutia, J. Ullrich, A laser ion source for an electron beam ion trap, Nuclear Instruments and Methods in Physics Research Section B: Beam Interactions with Materials and Atoms 251 (1) (2006) 289 – 296. doi:10.1016/j.nimb.2006.06.013.

[95] S. Nagy, private communication.

[96] A. Mooser, Der *g*-faktor des Protons, Ph.D. thesis, Johannes-Gutenberg Universität, Mainz (2013).

Erklärung:

Ich versichere, dass ich diese Arbeit selbstständig verfasst habe und keine anderen als die angegebenen Quellen und Hilfsmittel benutzt habe.

Heidelberg, den 23.Mai 2016 .....

Danksagung

An dieser Stelle möchte ich meinen Dank an verschiedene Personen ausdrücken:

Zuerst möchte ich mich bei Prof. Dr. Klaus Blaum bedanken für die Betreuung meiner Masterarbeit, die Unterstützung und immer freundlichen Umgang, sowie seine motivierende Art. Vielen Dank, dass du alles das ermöglicht hast.

Des Weiteren gilt mein größter Dank meinen Betreuern Dr. Sven Sturm und Dr. Robert Wolf, dass sie mir ihr so umfangreiches Wissen geduldig vermittelt haben und ich so unglaublich viel von ihnen lernen durfte. Der freundliche Umgang, die äußerst erleuchtenden Diskussionen, Unterstützung und gemeinsame schöne Zeit im Labor mit euch waren unheimlich motivierend.

Ebenso möchte ich mich bei Peter Micke bedanken, von dem ich bei der gemeinsamen Arbeit soviel über EBITs und speziell die tt-EBIT lernen konnte.

Bei Jochen Ketter möchte ich mich auch bedanken, für die vielen lehrreichen Diskussionen und dass du dir immer die Zeit nimmst einem so umfangreich und geduldig zu helfen.

Mein Dank gilt auch meinen Kollegen des Alphatrap Experiments für die schöne gemeinsame Zeit und den übrigen Kollegen der Abteilung für die freundliche Atmosphäre und gegenseitige Unterstützung. Besonders möchte ich Dr. Szilard Nagy für die Möglichkeit danken, dass ich mit ihm Messungen am TRIGA-TRAP Experiment machen konnte.

Natürlich möchte ich mich auch bei allen übrigen Kollegen des Instituts für die gute Zusammenarbeit bedanken.

Zum Schluss möchte ich meiner ganzen Familie danken. Vor allem danke ich meinen Eltern und meiner Schwester, für ihre bedingungslose Unterstüzung und Vertrauen, sowie ihre hingebungsvolle Liebe. Danke.